nature medicine

ARTICLES

https://doi.org/10.1038/s41591-020-1006-1

A peripheral immune signature of responsiveness to PD-1 blockade in patients with classical Hodgkin lymphoma

Fathima Zumla Cader[1,7,13], Xihao Hu[2,3,8,13], Walter L. Goh[4], Kirsty Wienand[1,9], Jing Ouyang[1], Elisa Mandato[1], Robert Redd[2], Lee N. Lawton[1], Pei-Hsuan Chen[5], Jason L. Weirather[5], Ron C. J. Schackmann[4,10], Bo Li[2,3,11], Wenjiang Ma[1,12], Philippe Armand[1], Scott J. Rodig[6], Donna Neuberg[2], X. Shirley Liu[2,3,14] ✉ and Margaret A. Shipp[1,14] ✉

PD-1 blockade is highly effective in classical Hodgkin lymphomas (cHLs), which exhibit frequent copy-number gains of *CD274* (*PD-L1*) and *PDC1LG2* (*PD-L2*) on chromosome 9p24.1. However, in this largely MHC-class-I-negative tumor, the mechanism of action of anti-PD-1 therapy remains undefined. We utilized the complementary approaches of T cell receptor (TCR) sequencing and cytometry by time-of-flight analysis to obtain a peripheral immune signature of responsiveness to PD-1 blockade in 56 patients treated in the CheckMate 205 phase II clinical trial (NCT02181738). Anti-PD-1 therapy was most effective in patients with a diverse baseline TCR repertoire and an associated expansion of singleton clones during treatment. CD4$^+$, but not CD8$^+$, TCR diversity significantly increased during therapy, most strikingly in patients who had achieved complete responses. Additionally, patients who responded to therapy had an increased abundance of activated natural killer cells and a newly identified CD3$^-$CD68$^+$CD4$^+$GrB$^+$ subset. These studies highlight the roles of recently expanded, clonally diverse CD4$^+$ T cells and innate effectors in the efficacy of PD-1 blockade in cHL.

CHLs include rare malignant Hodgkin Reed–Sternberg (HRS) cells admixed with abundant inflammatory and immune cells[1]. Although the cHL inflammatory infiltrate is rich in T cells, it is not associated with an effective antitumor immune response.

We previously identified near-universal copy-number gains of *PD-L1* and *PD-L2* on chromosome 9p24.1, and copy-number-dependent increased expression of the PD-1 ligands on HRS cells[2–5]. PD-1 ligands engage PD-1-receptor-positive T cells and induce T cell 'exhaustion', which can be abrogated by PD-1 blockade[6]. Patients with relapsed/refractory (R/R) cHL, who have a genetic basis for enhanced PD-1 signaling, also exhibit the highest reported response rates to PD-1 blockade[7–13]. As a consequence, multiple PD-1 antibodies have been approved for the treatment of R/R cHL and incorporated into frontline clinical trials[14,15]. Despite these genetic observations and rapid clinical translation, the precise mechanism of action of PD-1 blockade in cHL remains undefined.

In certain solid tumors, PD-1 blockade is reported to increase the activity of CD8$^+$ cytotoxic T cells in the tumor microenvironment (TME)[16–19]. However, HRS cells frequently lack cell-surface expression of β_2 microglobulin (B2M) and major histocompatibility complex (MHC) class I owing to inactivating mutations of *B2M* or copy loss of *B2M* or MHC class I genes[4,5,20,21]. As MHC-class-I-mediated tumor antigen presentation is essential for recognition by CD8$^+$ T cells, these findings implicate non-CD8$^+$ effector mechanisms of PD-1 blockade in cHL.

MHC-class-II-mediated antigen presentation to CD4$^+$ effector cells also plays an important role in antitumor immunity[22–27]. HRS cells are often MHC class II$^+$, likely reflecting their lineage from MHC class II$^+$ B cells in the germinal center[28,29]. In intact tumors, PD-L1$^+$ HRS cells are also more likely to be in physical contact with PD-1$^+$CD4$^+$ T cells than with PD-1$^+$CD8$^+$ T cells[30]. Our previous single-cell analyses of primary cHL cell suspensions also revealed a CD4$^+$ T-cell-rich TME with expanded numbers of T-helper 1 (T_H1)-polarized effectors and regulatory T cells[31].

Consistent with these observations, we also found that expression of MHC class II, but not MHC class I, in HRS cells was associated with responses to PD-1 blockade (nivolumab) in patients with R/R cHL[4]. Additional evidence of non-MHC-restricted immune mechanisms came from patients who achieved short-lived complete responses (CRs) to anti-PD-1 blockade although their HRS cells lacked expression of β2M, MHC class I and MHC class II[4].

Recent studies in murine models and patients with certain solid tumors associate circulating immune-cell subsets with responses to checkpoint blockade[32–38]. Herein, we utilized complementary approaches—TCR sequencing and cytometry by time-of-flight (CyTOF) analyses—to characterize the peripheral immune signature of patients with R/R cHL who received anti-PD-1 therapy.

[1]Department of Medical Oncology, Dana-Farber Cancer Institute, Boston, MA, USA. [2]Department of Data Sciences, Dana-Farber Cancer Institute, Boston, MA, USA. [3]Harvard T.H. Chan School of Public Health, Boston, MA, USA. [4]Department of Cell Biology, Harvard Medical School, Boston, MA, USA. [5]Center for Immuno-Oncology, Dana-Farber Cancer Institute, Boston, MA, USA. [6]Department of Pathology, Brigham and Women's Hospital, Boston, MA, USA. [7]Present address: AstraZeneca, City House, Cambridge, UK. [8]Present address: GV20 Therapeutics LLC, Cambridge, MA, USA. [9]Present address: Department of Hematology and Oncology, Göttingen Comprehensive Cancer Center, Göttingen, Germany. [10]Present address: Merus, Utrecht, the Netherlands. [11]Present address: Lyda Hill Department of Bioinformatics, UT Southwestern Medical Center, Dallas, TX, USA. [12]Present address: Clarion Healthcare, Boston, MA, USA. [13]These authors contributed equally: Fathima Zumla Cader, Xihao Hu. [14]These authors jointly supervised this work: X. Shirley Liu, Margaret A. Shipp. ✉e-mail: xsliu@ds.dfci.harvard.edu; Margaret_Shipp@dfci.harvard.edu

Results

Patient cohorts and samples. We obtained baseline and on-treatment peripheral blood mononuclear cell (PBMC) samples from 56 patients with recurrent cHL who were treated with nivolumab on the CheckMate 205 clinical trial and had best overall responses of CR, partial response (PR) or progressive disease (PD) (Supplementary Table 1)[8]. In this phase II study, patients who relapsed following autologous-stem-cell transplantation (ASCT) alone (Cohort A) or ASCT and brentuximab vedotin (BV) (Cohorts B and C)[8] received nivolumab (3 mg per kg body weight, intravenously (i.v.) every 2 weeks) until disease progression or unacceptable toxicity; patients in Cohort C who achieved a CR discontinued nivolumab following 1 yr of therapy[8].

PBMCs from trial patients were collected immediately before the initiation of therapy (cycle 1 day 1 (C1D1)) and at two timepoints during PD-1 blockade, cycle 2 day 1 (C2D1) and cycle 4 day 1 (C4D1). PBMCs were also obtained from patients with newly diagnosed, previously untreated cHL and healthy donors for comparisons (Methods and Supplementary Table 1).

Analyses of baseline TCR diversity. We first sequenced the complementarity-determining region 3 (CDR3) regions on the TCR beta chain from all PBMC samples and analyzed TCR repertoire diversity using the Shannon entropy index (Methods). Baseline TCR diversity was significantly higher in normal healthy donors than in patients with newly diagnosed cHL ($P = 4.4 \times 10^{-5}$), indicating that these patients have a reduced TCR repertoire prior to the initiation of therapy (Fig. 1a). Additionally, TCR diversity was significantly higher in patients with newly diagnosed cHL than in patients with R/R disease ($P = 0.00083$), potentially reflecting disease progression and/or prior treatment (Fig. 1a).

The loss of TCR diversity in patients with R/R disease (Fig. 1a) prompted us to assess a potential association between baseline TCR repertoire and subsequent response to PD-1 blockade (Fig. 1b). Earlier analyses suggested that functional T cell recovery requires ≥1 yr following myeloablative therapy and ASCT[4,39–41]. For this reason, we separately analyzed patients who began nivolumab therapy <1 or ≥1 yr after myeloablative ASCT (Fig. 1b). As expected, patients who were <1 yr from prior ASCT had lower baseline TCR diversity (Fig. 1b). To avoid the confounding variable of ongoing immune reconstitution, we restricted our subsequent analyses to patients who were treated with nivolumab ≥1 yr following myeloablative ASCT. The number of prior therapies was not significantly different in these trial patients, although those who progressed on nivolumab had higher median values (Extended Data Fig. 1a). The percentages of circulating T cells and numbers of detected TCR sequences at baseline were not significantly different in these trial patients (Extended Data Fig. 1b–d).

Baseline TCR diversity in patients with R/R disease who achieved a CR with nivolumab was not significantly different from that in newly diagnosed patients ($P = 0.27$, Fig. 1b); in contrast, baseline TCR diversity was significantly lower in the patients with R/R disease who obtained only a PR ($P = 0.00024$) or had PD ($P = 0.013$) following PD-1 blockade (Fig. 1b).

In our earlier studies of the CheckMate 205 patients, HRS cell expression of MHC class II, but not MHC class I, was associated with response to PD-1 blockade[4]. Additionally, we previously found that the cHL TME was enriched for CD4+ cells, including those in immediate proximity to HRS cells[30,31]. These findings prompted us to perform TCR sequencing of highly purified peripheral CD4+ and CD8+ T cells and assess their respective repertoires in healthy donors, patients with newly diagnosed cHL and trial patients with R/R cHL who were treated with nivolumab beginning ≥1 yr after ASCT at baseline and following PD-1 blockade (Fig. 1c–f). The trial patients had no significant differences in ratios of input CD4+ and CD8+ T cells or total detected CD4+ and CD8+ TCR sequences at baseline (Extended Data Fig. 1e–h).

Peripheral CD4+ TCR repertoire diversity was significantly higher in healthy donors than in patients with newly diagnosed or R/R cHL ($P = 0.00028$ and $P = 1.1 \times 10^{-6}$, respectively, Fig. 1c). Whereas baseline CD4+ TCR diversity was not significantly different in newly diagnosed patients and those with R/R disease who obtained subsequent CRs to nivolumab ($P = 0.065$), it was significantly lower in patients with PRs or PD ($P = 0.014$ and $P = 0.0024$, respectively, Fig. 1d). Similar patterns were observed in baseline CD8+ TCR diversity; however, Shannon indices were lower in CD8+ than CD4+ subsets (Fig. 1c–f).

After characterizing baseline differences in CD4+ and CD8+ TCR diversity in trial patients, we assessed dynamic changes in these repertoires following PD-1 blockade (C1D1 to C4D1, Fig. 1g,h). Following 6 weeks of therapy (C4D1), there was a highly significant increase in CD4+, but not CD8+, TCR repertoire diversity ($P = 0.0027$ and $P = 0.16$, respectively, Fig. 1g). In addition, the selective increase in CD4+ TCR repertoire diversity was most apparent in patients who achieved CRs to nivolumab ($P = 0.02$, Fig. 1h). Furthermore, in the subset of patients whose HRS cells were previously characterized for MHC class I and MHC class II expression[4], only those with MHC class II+ tumor cells had significantly increased TCR repertoire diversity following PD-1 blockade (Extended Data Fig. 1i,j). These data highlight the importance of a CD4+ T cell response to PD-1 blockade in this lymphoid malignancy, which is largely MHC class I negative.

Clonal T cell expansion following PD-1 blockade. We postulated that TCR diversity, which reflects the number of individual T cell clones capable of recognizing distinct antigens, would align with peripheral T cell differentiation in our trial patients. For this reason, we used our recently described CyTOF panel[31] (Methods) to identify CD3+ naive, central memory (CM), effector memory (EM) and terminally differentiated effector memory (TEMRA) T cells on the basis of their expression of CCR7 and CD45RO (Fig. 2a).

We reasoned that singleton TCR clones, which appeared only once in TCR sequencing, were more likely to represent peripheral T cells that had not yet encountered an antigen or had undergone limited clonal expansion. To assess this, we compared the TCR sequencing (TCR-seq)-measured ratio of singleton/all clones with the CyTOF-determined ratio of naive, CM, EM or TEMRA T cells/all T cells in trial patients (Fig. 2b). In all CD3+ T cells and purified CD4+ and CD8+ T cell subsets, the relative abundance of singleton clones was more closely associated with that of naive and central memory T cells (Fig. 2b, top and bottom). These data suggest that T cells with singleton TCRs are less likely to be terminally differentiated.

Given the association between increased TCR repertoire diversity and response to PD-1 blockade (Fig. 1g,h), we next evaluated clonal T cell expansion following therapy. In patients who were treated with nivolumab ≥1 yr after ASCT, we identified 4,045,691 unique TCR sequences at baseline; 792,705 of these TCR clones expanded by at least twofold following treatment (Fig. 2c) (Methods).

We compared the expansion of T cell clones derived from singletons (zero or one copy pretreatment) or non-singletons (two or more copies pretreatment) and assessed the ratio of expanded singleton over non-singleton T cells following PD-1 blockade (Fig. 2d–f). Patients who achieved a CR exhibited significantly greater expansion of singleton over non-singleton clones, in comparison with those who obtained only a PR or PD (Fig. 2d–f and Extended Data Fig. 1k). These data indicate that clonal expansion of less terminally differentiated singletons, rather than non-singletons, is associated with a favorable response to PD-1 blockade in cHL. Similar results were seen in purified CD4+ singleton over non-singleton clones and, to a lesser extent, in CD8+ TCR subsets (Extended Data Fig. 1l,m).

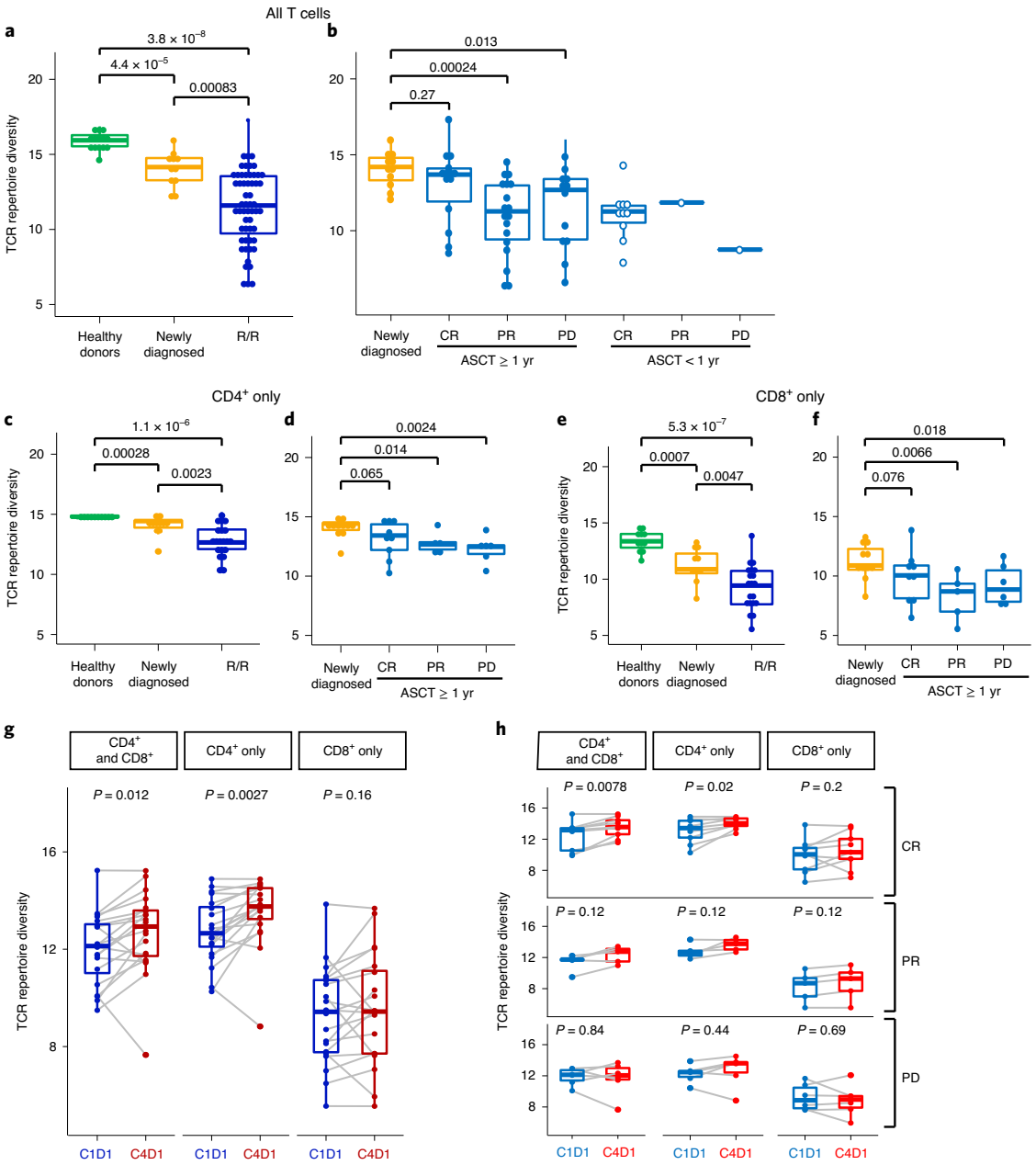

Fig. 1 | Analyses of peripheral TCR repertoire diversity at baseline and following PD-1 blockade. a, TCR repertoire diversity, as determined by the Shannon diversity index, in healthy donors ($n=14$) and patients with newly diagnosed ($n=11$) or R/R ($n=56$) cHL. **b**, TCR repertoire diversity in patients with R/R cHL separated by subsequent response to PD-1 blockade (CR, PR and PD) and time interval between prior myeloablative ASCT (<1 yr versus ≥1 yr) and initiation of anti-PD-1 treatment. Patients with CR and ASCT ≥ 1 yr ($n=14$); PR and ASCT ≥ 1 yr ($n=18$); PD and ASCT ≥ 1 yr ($n=12$); CR and ASCT < 1 yr ($n=10$); PR and ASCT < 1 yr ($n=1$); and PD and ASCT < 1 yr ($n=1$). Patients with newly diagnosed cHL included for comparison. Analyses in **a** and **b** were done by Wilcoxon rank-sum tests with two-sided *P* values. **c**–**f**, TCR repertoire diversity in CD4$^+$ (**c**,**d**) or CD8$^+$ (**e**,**f**) peripheral T cells from healthy donors ($n=13$), patients with newly diagnosed ($n=11$) or R/R cHL and ASCT ≥ 1 yr prior to anti-PD-1 therapy ($n=20$, including 9 CRs, 5 PRs and 6 PDs). Analyses were done by Wilcoxon rank-sum tests with one-sided *P* values. **g**, Changes in TCR repertoire diversity following PD-1 blockade (cycle 1 day 1 (C1D1) to cycle 4 day 1 (C4D1)). In patients with R/R cHL and ASCT ≥ 1 yr prior to anti-PD-1 therapy, changes in TCR diversity between C1D1 and C4D1 were evaluated in combined CD4$^+$ and CD8$^+$, CD4$^+$ only and CD8$^+$ only peripheral T cells from a subset of patients with available paired samples ($n=20$, all). **h**, Changes in TCR diversity following PD-1 blockade (C1D1 to C4D1) in patients (from **g**) separated by best overall response (BOR) to treatment (CRs, $n=9$; PRs, $n=5$; and PDs, $n=6$). Analyses were done by Wilcoxon rank-sum tests with two-sided *P* values in **g** and **h**. For all box plots, the lower and upper hinges correspond to the 25th and 75th percentiles. The whiskers extend from the largest to smallest value, but no further than 1.5 times the interquartile range (IQR), with outliers plotted individually.

CD3$^+$ cells in healthy donors and patients with newly diagnosed cHL. We next used CyTOF to characterize peripheral CD3$^+$ cell types in three scenarios: healthy donors and patients with newly diagnosed cHL (Fig. 3a–c and Fig. 4a); patients with newly diagnosed and R/R cHL at baseline (Fig. 3f–h and Fig. 4b); and patients with R/R cHL at baseline and following PD-1 blockade (Fig. 4e,f). These cohorts were analyzed separately to maximize resolution of distinct immune clusters.

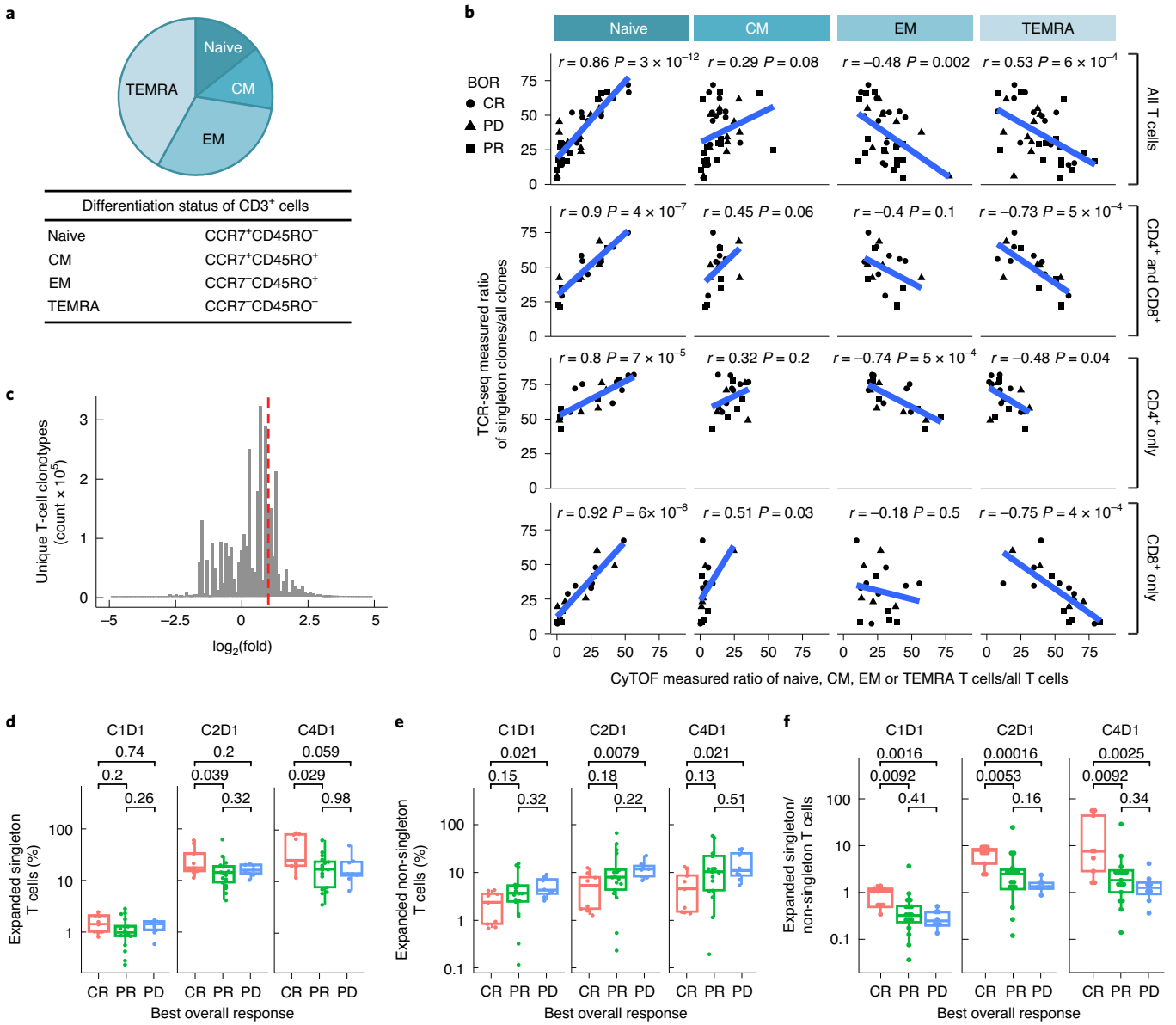

Fig. 2 | Clonal expansion following PD-1 blockade. a, The median CyTOF-based measurement of CD3+ T cell differentiation subsets (naive, CM, EM and TEMRA) in patients with R/R cHL and ASCT ≥1 yr prior to anti-PD-1 treatment ($n = 38$ total). **b**, Correlation between the relative abundance of TCR-seq-measured singleton clones (ratio of singleton clones/all clones) and relative abundance of CyTOF-defined T cell differentiation subsets (ratio of naive, CM, EM or TEMRA/all T cells). Analyses were performed in all CD3+ T cells (top, $n = 38$); the combination of sorted CD4+ and CD8+ T cells (upper middle); CD4+ T cells only (lower middle); and CD8+ T cells only (bottom) (CD4+ and CD8+, CD4+ only and CD8+ only, $n = 20$). The Pearson's correlation was applied, and the two-sided P value was estimated by a T distribution. **c**, Unique T cell clonotypes in patients with R/R cHL treated with PD-1 blockade. All patients in the analysis began nivolumab treatment ≥1 yr following myeloablative therapy and ASCT. TCR sequences (clonotypes) from baseline (C1D1) and on-treatment (C2D1 and C4D1) samples. The area to the right of the dotted red line denotes T cell clonotypes with twofold or greater expansion following treatment. Clonotypes at zero or below are unchanged or decreased/lost with treatment. The distribution is for 4,045,691 clonotypes from the 34 trial patients with available samples from all 3 timepoints (C1D1, C2D1 and C4D1). **d**–**f**, The percentage expansion of singleton clones (zero or one copy at baseline) (**d**) and non-singleton clones (two or more copies at baseline) (**e**), and the ratio of expanded singleton/non-singleton clones (**f**), in patients with CR, PR or PD to PD-1 blockade. Only patients with samples at all 3 timepoints ($n = 34$) were included in the analysis. C1D1 shows baseline (pretreatment) levels of clones that subsequently expand at C2D1 and C4D1. Patients with CR to PD-1 blockade have significantly greater expansion of singleton, as opposed to non-singleton, clones (Wilcoxon rank-sum test with two-sided P values). For all box plots, the lower and upper hinges correspond to the 25th and 75th percentiles. The whiskers extend from the largest to smallest value, but no further than 1.5 times the IQR, with outliers plotted individually.

An equivalent number of single cells from each sample were analyzed and clustered with the VorteX/X-shift algorithms and visualized in a force-directed layout (FDL) (Methods)[31,42]. The FDL of viable peripheral CD3+ cells from healthy donors and patients with newly diagnosed cHL revealed individual clusters (Fig. 3a) arranged into larger groups defined by known cell lineage markers, CD3+, CD4+ and CD8+ (Fig. 3b), and additional markers of differentiation, polarization and function (Extended Data Fig. 2a). For downstream analyses, we focused on major clusters with at least 100 cells in ≥10% of samples and evaluated the relative expression of CyTOF

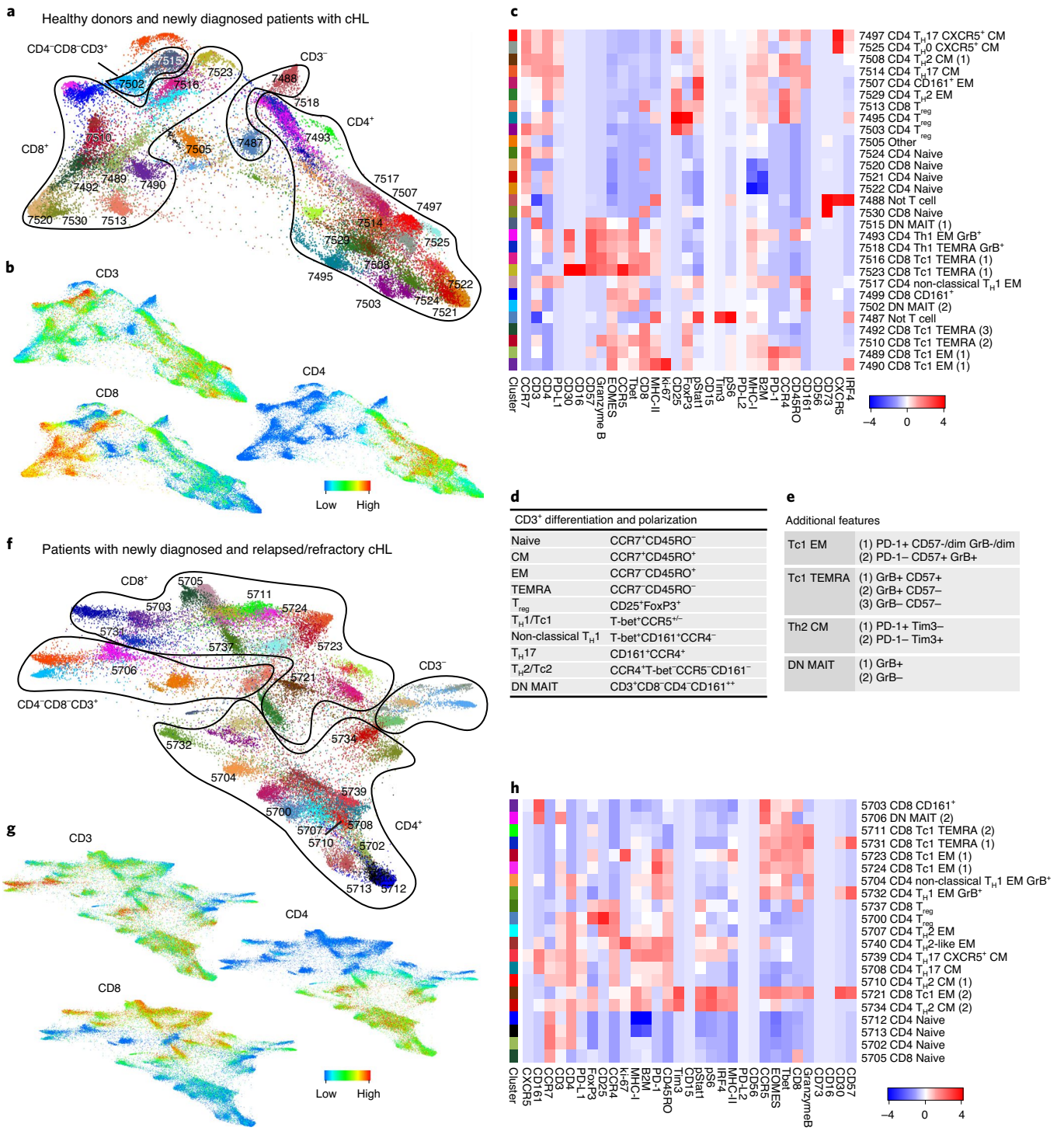

d

$CD3^+$ differentiation and polarization	
Naive	$CCR7^+CD45RO^-$
CM	$CCR7^+CD45RO^+$
EM	$CCR7^-CD45RO^+$
TEMRA	$CCR7^-CD45RO^-$
T_{reg}	$CD25^+FoxP3^+$
T_H1/Tc1	$T\text{-}bet^+CCR5^{+/-}$
Non-classical T_H1	$T\text{-}bet^+CD161^+CCR4^-$
T_H17	$CD161^+CCR4^+$
T_H2/Tc2	$CCR4^+T\text{-}bet^-CCR5^-CD161^-$
DN MAIT	$CD3^+CD8^-CD4^-CD161^{++}$

e

Additional features	
Tc1 EM	(1) PD-1+ CD57-/dim GrB-/dim (2) PD-1− CD57+ GrB+
Tc1 TEMRA	(1) GrB+ CD57+ (2) GrB+ CD57− (3) GrB− CD57−
Th2 CM	(1) PD-1+ Tim3− (2) PD-1− Tim3+
DN MAIT	(1) GrB+ (2) GrB−

Fig. 3 | Analyses of circulating $CD3^+$ cells in healthy donors and patients with newly diagnosed or R/R cHL. a, FDL of circulating $CD3^+$ cells from healthy donors and newly diagnosed patients with cHL. For $CD3^+$ cell analyses, all antibody channels except PAX5, CD163, CD68, CD33 and CD14 were included. Each unique population (cluster) is labeled with a distinct color and identified by a unique number. **b**, Major lineages in **a** defined by expression of CD3, CD4 and CD8. **c**, Heatmap showing relative expression of CyTOF panel proteins in clusters with >100 cells in ≥10% of samples from **a**. DN, double negative; Tcl, T cytotoxic 1. **d**, Markers used to identify major $CD3^+$ subsets. T-bet, T-box transcription factor TBX21. **e**, Markers used to define polarization, differentiation and functional status. **f**, FDL of circulating $CD3^+$ cells from patients with newly diagnosed and those with R/R cHL. **g**, Expression of CD3, CD4 and CD8 in **f**. **h**, Heatmap showing relative expression of CyTOF panel proteins in clusters with >100 cells in ≥10% of samples from **f**. For inclusion in the analyses of $CD3^+$ clusters in healthy donors ($n=11$) and patients with newly diagnosed cHL ($n=9$) in **a**, available samples must have had 12,000 sampled events. For inclusion in the analyses of $CD3^+$ clusters in patients with newly diagnosed cHL ($n=9$) and R/R cHL ($n=36$) in **f**, available samples must have had 7,500 sampled events.

panel proteins with a heatmap (Fig. 3c). Thereafter, we manually annotated the identified clusters using additional lineage, differentiation, polarization and functional markers (Fig. 3c–e).

CD4$^+$ and CD8$^+$ T cells were then identified as naive, CM, EM or TEMRA cells on the basis of CCR7 and CD45RO expression (Fig. 3d); regulatory T cells (T_{reg}s) were defined as CD25$^+$ and FoxP3$^+$ (Fig. 3d). As expected, we detected CD4$^+$ and CD8$^+$ naive T cell clusters (cluster ID nos. 7524, 7521, 7522 and 7520); however, in the absence of local cytokine gradients, there was less polarization of circulating CD4$^+$ T cell subsets (CM, EM, TEMRA and T_{reg}) (Fig. 3c,d) than in previously characterized primary cHL cell suspensions[31]. PD-1 was largely expressed on CD8$^+$ and CD4$^+$ EM cells, including circulating CD4$^+$ T_H1 granzyme B$^+$ (GrB$^+$) cytotoxic T cells (ID no. 7493) (Fig. 3c). CD4$^+$ CM cells (ID nos. 7508 and 7514) had lower levels of PD-1, and CD4$^+$ and CD8$^+$ T_{reg}s were PD-1$^-$ (IDs nos. 7495, 7503 and 7513). We also identified CD3$^+$CD4$^-$CD8$^-$ subsets that expressed CD161 with or without GrB (ID nos. 7515 and 7502) (Fig. 3e). These CD161$^+$ cells may represent mucosal-associated invariant (MAIT) cells, which have a limited TCR repertoire and innate-like effector responses[43].

CD3$^+$ T cells in patients with newly diagnosed and R/R cHL. We similarly analyzed CD3$^+$ PBMCs from patients with newly diagnosed and R/R cHL (at baseline) (Fig. 3f,g and Extended Data Fig. 2b). Focusing again on the major clusters with at least 100 cells in ≥10% of samples, we identified comparable CD3$^+$ subsets including CD4$^+$ T_H1 GrB$^+$ PD-1$^+$ cells (ID nos. 5704 and 5732) (Fig. 3h). PD-1 was expressed on CD8$^+$ (ID nos. 5723 and 5724) and CD4$^+$ EM cells (ID nos. 5704, 5732 and 5740) with lower levels on CD4$^+$ CM cells (ID no. 5734) (Fig. 3h). We also detected a likely GrB$^-$CD161$^+$ MAIT-cell subset (ID no. 5706) (Fig. 3h).

Comparative analyses of CD3$^+$ clusters in healthy donors and patients with newly diagnosed and R/R cHL. The median cluster cell counts in healthy donors versus newly diagnosed patients (Extended Data Fig. 3) and newly diagnosed patients versus those with R/R disease (Extended Data Fig. 4) were calculated and displayed as comparison bar graphs (healthy donors versus newly diagnosed cHL, Fig. 4a and newly diagnosed versus R/R cHL, Fig. 4b) with highlighted significant differences and relative levels of PD-1 expression (Fig. 4a,b, right panels).

In comparison with healthy donors, patients with newly diagnosed cHL had significantly fewer peripheral CD8$^+$ naive cells ($P=0.0074$) but similar numbers of CD4$^+$ naive cells ($P=0.7664$) (Fig. 4a,c,d, left panel). Although patients with newly diagnosed and R/R cHLs had similar numbers of peripheral CD8$^+$ naive cells ($P=0.2928$) (Fig. 4b,c, right panel), patients with R/R cHL had significantly fewer peripheral CD4$^+$ naive cells ($P<0.0001$) (Fig. 4b,d, right panel) and increased numbers of more differentiated CD4$^+$ and CD8$^+$ effector T cell subsets that were largely PD-1$^+$ with higher relative levels of PD-1 expression (Fig. 4b and Extended Data Fig. 4d).

Given the decreased number of CD3$^+$ naive cells in patients with R/R cHL at baseline (Fig. 4c,d, right panels, and Extended Data Fig. 5), we also assessed naive T cell numbers following PD-1 blockade (C4D1, Fig. 4e,f). Patients with higher numbers of naive T cells at C4D1 had more favorable responses to nivolumab treatment (C4D1 CD8$^+$ naive T cells, CR > PR > PD $P=0.012$ (Fig. 4e) and C4D1 CD4$^+$ naive T cells, CR > PR > PD $P=0.021$ (Fig. 4f)). These findings align with the response-related differences in TCR repertoire diversity and singleton clonal T cell expansion during treatment (Fig. 1g,h and Fig. 2f, respectively), and likely reflect continued capacity to generate new immune responses.

CD3$^-$ cells in healthy donors, patients with newly diagnosed cHL and patients with R/R cHL. We similarly analyzed peripheral CD3$^-$ subsets, including B cells, monocytes and natural killer (NK) cells, using CyTOF. In healthy donors and patients with newly diagnosed cHL, the associated FDL included individual clusters arranged into larger groups of B cells (PAX5/MHC class II), monocytes (CD33/CD14/CD16) and NK cells (CD56) (Fig. 5a,b). The major clusters (≥100 cells in ≥10% of samples) were evaluated for the relative expression of CyTOF panel proteins (Fig. 5c) and defined by their phenotype (Fig. 5d,e): classical monocytes, CD33$^+$CD14$^+$CD16$^-$; non-classical monocytes, CD33$^+$CD14$^-$CD16$^+$; intermediate monocytes, CD14$^+$CD16$^+$; monocytic dendritic cells, CD33$^+$CD14$^-$CD16$^-$MHC class II$^+$; and neutrophils, CD15$^+$CD16$^+$ (ref. [44]). B cell clusters expressed PAX5 and MHC class II with or without CXCR5, CD73 and IRF4. NK cell clusters were defined by the expression of CD56, four additional markers—CD16, CD57, GrB and CD161—that reflected stages of NK cell differentiation (CD56^{bright}, CD56$^{+/immature}$, CD56$^{+/mature}$ and adaptive)[45] and EOMES (Fig. 5d,e). We also detected a CD56$^+$CD16$^+$PD-1$^+$GrB$^-$ cluster (ID no. 6661) at a distance from other NK cell clusters on the FDL and a discrete CD3$^-$ CD68$^+$CD4$^+$GrB$^+$ subset that lacked expression of other monocyte markers (ID no. 6615) (Fig. 5a,c,d).

In patients with newly diagnosed and R/R cHL (at baseline) (Fig. 5f), the CD3$^-$ subsets were largely analogous to those in

Fig. 4 | Comparative analyses of CD3$^+$ clusters in healthy donors and patients with newly diagnosed and R/R cHL. a,**b**, To quantify the immune-cell clusters in each group, we calculated the median cluster cell counts in healthy donors versus newly diagnosed patients and newly diagnosed patients and those with R/R cHL. Results are displayed in comparison bar graphs (healthy donors versus newly diagnosed cHL, **a**; newly diagnosed versus R/R cHL, **b**). Significant differences (Wilcoxon rank-sum test with nominal two-sided $P \leq 0.05$) and directions of the differences are shown on the right. *P* values that remained significant after Benjamini–Hochberg correction are noted (*). See also Extended Data Figs. 3a,b and 4a,b for exact *P* values. Relative levels of PD-1 expression in specific clusters are visually represented alongside each bar graph in **a** and **b** (far right). See also Extended Data Fig. 4d. **a**, Healthy donors versus patients with newly diagnosed cHL. **b**, Patients with newly diagnosed cHL versus patients with R/R cHL. **c**, CD8$^+$ naive T cell counts at baseline in healthy donors versus newly diagnosed patients (left) and patients with new diagnosed versus R/R cHL (right). **d**, CD4$^+$ naive T cell counts at baseline in healthy donors versus newly diagnosed patients (left) and patients with new diagnosed versus R/R cHL (right). **e**, CD8$^+$ naive T cell counts post-treatment (C4D1), by best overall response (BOR) to PD-1 blockade. **f**, CD4$^+$ naive T cell counts post-treatment (C4D1) by BOR. In **c** and **d**, differences between groups were assessed with Wilcoxon rank-sum tests with nominal two-sided *P* values. A Benjamini–Hochberg correction was applied in CD3$^+$CD4$^+$ and CD3$^+$CD8$^+$ cell types, and nominal *P* values that retain significance are noted (with an asterisk). In **e** and **f**, a Cuzick trend test was used to compare across the groups, and two-sided nominal *P* values are shown. All box plots (generated in GraphPad Prism) define the 25th and 75th percentiles and median values, and whiskers show the minimum and maximum values. In these analyses, clusters with similar phenotypes, such as CD4$^+$ naive clusters 7524, 7521 and 7522, were collapsed. For inclusion in the analyses of CD3$^+$ clusters in healthy donors ($n=11$) and patients with newly diagnosed cHL ($n=9$) in **a**, available specimens must have had 12,000 sampled events. For inclusion in the analyses of CD3$^+$ clusters in patients with newly diagnosed cHL ($n=9$) and R/R cHL ($n=36$) in **b**, available specimens must have had 7,500 sampled events. For inclusion in the post-treatment C4D1 analysis of R/R cHLs ($n=29$; CR = 9, PR = 15 and PD = 5) in **e** and **f**, available specimens must have had 7,500 sampled events, and included patients must also have had a baseline sample. Six patients with R/R cHL who had sufficient events for the baseline analysis in **b** had no C4D1 sample; one patient who had sufficient events for the baseline analysis in **b** had <7,500 sampled events at C4D1 and was excluded from the C4D1 analyses in **e** and **f**.

the healthy donors and newly diagnosed patients albeit with fewer B⁻cell and monocyte clusters (Fig. 5h). NK cell clusters with features resembling CD56^{bright}, CD56$^{+/immature}$, CD56$^{+/mature}$ and adaptive subsets were also identified (Fig. 5e,f,h). As in healthy donors and newly diagnosed patients (Fig. 5a,c), we detected a CD56⁺CD16⁺PD-1⁺GrB⁻ cluster (ID no. 705) that was distinct from other NK subsets and a CD3⁻ CD68⁺ CD4⁺ GrB⁺ subset (ID no. 729) (Fig. 5f,h).

Comparative analyses of CD3⁻ clusters in healthy donors and patients with newly diagnosed and R/R cHL. We next quantified the differences in abundance of the CD3⁻ clusters in healthy

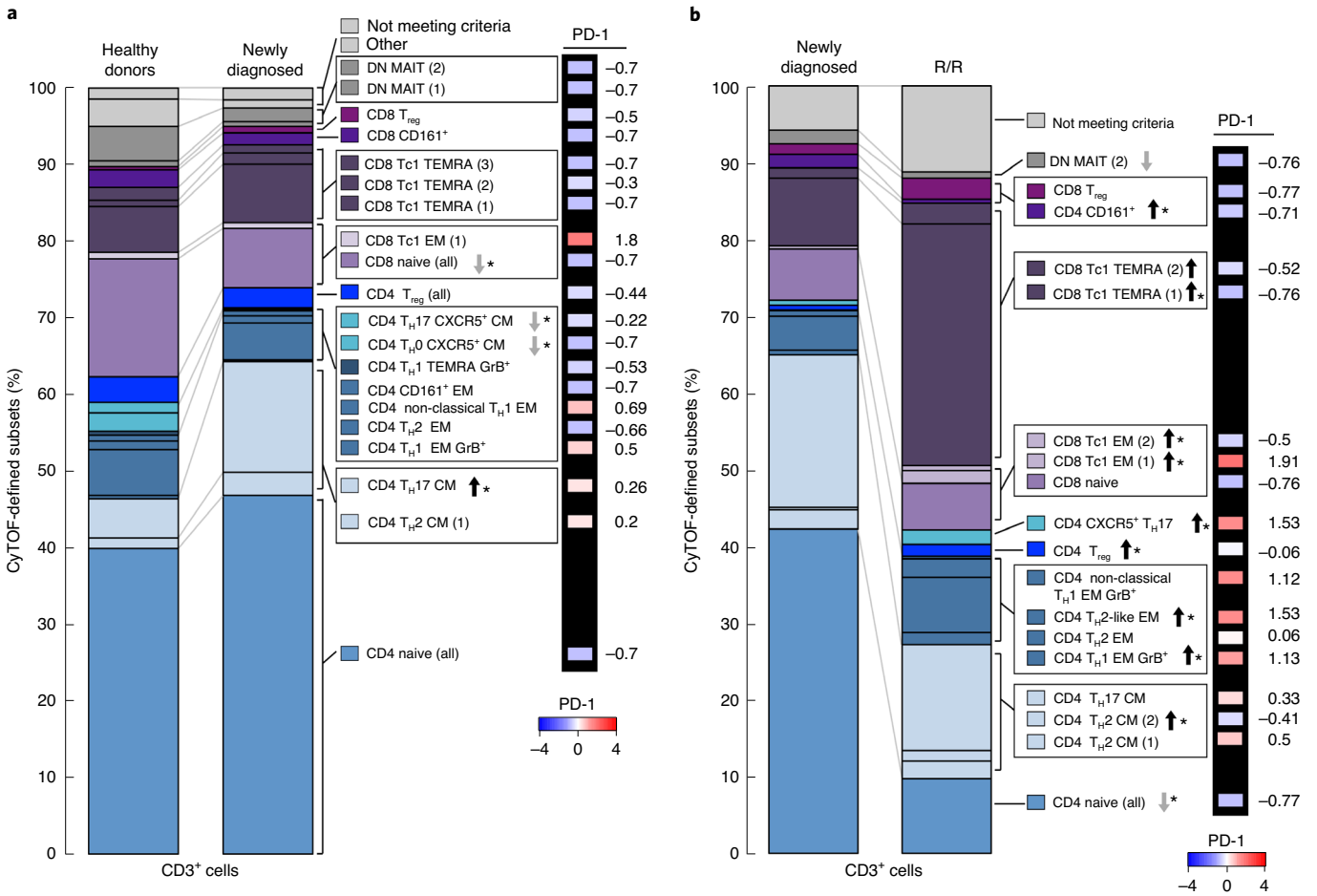

donors versus newly diagnosed patients (Extended Data Fig. 6) and newly diagnosed patients versus those with R/R disease (Extended Data Fig. 7) and displayed these data in comparison bar graphs (healthy donors versus newly diagnosed patients, Fig. 6a, and newly diagnosed versus R/R patients, Fig. 6b), with highlighted statistically significant differences. In comparison to healthy donors, patients with newly diagnosed cHL had expanded numbers of classical monocytes (Fig. 6a,c, left panel, $P=0.0021$) and neutrophils (Fig. 6a and Extended Data Fig. 6c), and a highly significant loss of B cells (Fig. 6a,d, left panel, B cells (all), ($P<0.0001$)) and normal NK cells at all stages of differentiation (NK1, $CD56^{bright}$ ($P=0.0017$); NK2, $CD56^{+/immature}$ ($P=0.041$); NK3, $CD56^{+/mature}$ (all) ($P<0.0001$); and NK4, adaptive ($P<0.0001$)) (Fig. 6a,e). These circulating NK cell subsets were largely PD-1$^-$, in contrast with results in a prior report[46]. Notably, the newly identified and potentially dysfunctional $CD56^+CD16^+PD\text{-}1^+GrB^-$ cell population was absent in healthy donors and only detected in patients with newly diagnosed cHL ($P=0.0001$) (Fig. 6a,g). The $CD3^-CD68^+CD4^+GrB^+$ subset was significantly more abundant in healthy donors than in newly diagnosed patients (Fig. 6a,h, left panel, $P=0.018$).

There were less striking differences in the abundance of specific CD3$^-$ subsets when patients with newly diagnosed cHL were compared to the entire group with R/R disease (Fig. 6b). However, among patients with R/R cHL, baseline differences in the abundance of certain CD3$^-$ subsets were associated with subsequent response to PD-1 blockade. Specifically, patients with fewer circulating classical monocytes and more abundant B cells, mature NK cells and $CD3^-CD68^+CD4^+GrB^+$ cells had more favorable responses to PD-1 blockade (classical monocytes, CR < PR < PD $P=0.058$, Fig. 6c, right panel; B cells, CR > PR > PD $P=0.052$, Fig. 6d, right panel; $CD56^{+/mature}$ NK cells, CR > PR > PD $P=0.027$, Fig. 6f; and $CD3^-CD68^+CD4^+GrB^+$ cells, CR > PR > PD $P=0.026$, Fig. 6h, right panel and Extended Data Fig. 8). Patients who achieved a CR to nivolumab had CD3$^-$ peripheral immune signatures that more closely resembled those of healthy donors (Fig. 6c–f,h), suggesting that the relative composition of circulating CD3$^-$ cells may be more important than the abundance of a single CD3$^-$ subtype[35].

The peripheral immune signatures highlighted the potential role of two innate populations—NK cells and $CD3^-CD68^+CD4^+GrB^+$ cells—in the cytotoxic response to PD-1 blockade (Fig. 6f,h, right panel). As the circulating $CD3^-CD68^+CD4^+GrB^+$ subset was newly identified, we queried our earlier CyTOF analyses of primary cHLs[31] and detected cells with the same phenotype in the inflammatory infiltrate (Fig. 6i and Extended Data Fig. 9). These $CD3^-CD68^+CD4^+GrB^+$ cells also expressed IRF4, pSTAT1 and pS6, suggesting prior exposure to interferon-γ (Fig. 6i). In complementary studies, we used multiparametric immunofluorescence to assess the presence and frequency of $CD3^-CD68^+CD4^+GrB^+$ cells in intact tumor biopsies from 4 additional patients with relapsed cHL (Fig. 6j); in these cases, 22.7% (±3.1), 11% (±1.3), 9.2% (±1.2) and 2% (±1) of all $CD68^+$ cells were $CD3^-CD4^+GrB^+$. Together, these data define an additional innate GrB^+ cell population associated with favorable response to PD-1 blockade in cHL (Fig. 6h–j).

Discussion

We used TCR sequencing and CyTOF analysis to define a peripheral immune signature associated with response to PD-1 blockade in patients with R/R cHL. To provide context, we similarly characterized the circulating immune signature in patients with newly diagnosed cHL and healthy donors. In comparison with healthy donors, patients with newly diagnosed cHL had a significantly reduced TCR repertoire; patients with R/R cHL had an even greater decrease in TCR diversity. In patients with R/R cHL who received nivolumab, bulk and $CD4^+$-specific TCR diversity at baseline and during therapy were associated with response. Bases for the observed differences in TCR repertoire remain to be defined and potentially include disease activity and prior therapy. The current study is also limited to a single clinical trial cohort.

In comparison with healthy donors and patients with newly diagnosed cHL, those with R/R disease had significantly fewer peripheral $CD3^+$ naive T cells and greater numbers of differentiated $CD4^+$ and $CD8^+$ effector cells that were largely PD-1^+. Similar results—decreased numbers of circulating $CD4^+$ and $CD8^+$ naive cells and increased percentages of differentiated effectors—have been described in certain solid tumors[36]. Previous studies revealed the limited capacity of terminally differentiated exhausted T cells to respond to PD-1 blockade due to a fixed epigenetic profile[47,48]. Additionally, emerging data suggest that stem-like T cells with low or no expression of checkpoint receptors are needed to respond to PD-1 blockade[49–53]. In our trial patients with cHL, PD-1 blockade was more effective in those who had a diverse peripheral TCR repertoire and an associated expansion of singleton T cell clones during therapy.

Our findings align with those in patients with solid tumors whose responses to PD-1 blockade were more dependent upon the recruitment of new T cell clones than on the further expansion of previously identified tumor-specific T cells[53,54]. In cHL, which has a high tumor mutational burden[5] and a T-cell-rich inflammatory infiltrate, PD-1 blockade may facilitate T cell responses to new neoantigens.

After 6 weeks of PD-1 blockade, there was a highly significant increase in $CD4^+$, but not $CD8^+$, TCR diversity; additionally, these $CD4^+$-selective changes were most striking in patients with the best responses (CRs) to treatment. These findings directly implicate the $CD4^+$ T cell axis in the response to PD-1 blockade in cHL. In this tumor with frequent MHC class I loss, $CD4^+$ T cells may function directly as cytotoxic effectors. In this regard, we identified candidate circulating $CD4^+$ cytotoxic T cells ($CD4^+GrB^+PD\text{-}1^+$ T_H1 EM cells) that were more abundant in patients with R/R cHL than in those with newly diagnosed disease.

However, our data also prompt speculation regarding $CD4^+$ T cell modulation of innate cytotoxic effectors. In comparison with normal healthy donors, patients with newly diagnosed cHL had significantly fewer circulating NK cells at all stages of differentiation. Among patients with R/R cHL, the relative abundance of mature NK cells was also associated with response to PD-1 blockade[4,21]. Previous studies highlighted the synergy between $CD4^+$ T cell and NK cell antitumor responses[55], the role of impaired $CD4^+$ T cells in NK cell dysfunction and the benefit of PD-1 blockade in improving $CD4^+$ T cell and NK cell cooperation, in part via

Fig. 5 | Analyses of circulating CD3$^-$ cells in healthy donors and patients with newly diagnosed or R/R cHL. a, FDL of circulating CD3$^-$ cells from healthy donors and newly diagnosed patients with cHL. Every unique population (cluster) is labeled with a distinct color. **b**, Major lineages in **a** defined by expression levels of key markers: PAX5, MHC class II (B cells); CD33, CD14, CD16, MHC class II (monocytes); and CD56, CD16 (NK cells). **c**, Heatmap showing relative expression of CyTOF panel proteins in clusters with >100 cells in ≥10% of samples from **a**. **d**, Markers used to identify major CD3$^-$ subsets. **e**, Markers used to characterize NK stages of differentiation. **f**, FDL of circulating CD3$^-$ cells from patients with newly diagnosed and R/R cHL. **g**, Major lineages in **f** defined by expression of the indicated markers (as in **b**). **h**, Heatmap showing relative expression of CyTOF panel proteins in clusters with 100 cells in ≥10% of samples in **f**. For inclusion in the analyses of CD3$^-$ clusters in healthy donors ($n=11$) and patients with newly diagnosed cHL ($n=10$) in **a**, available specimens must have had 12,000 sampled events. For inclusion in the analyses of CD3$^-$ clusters in patients with newly diagnosed cHL ($n=10$) and R/R cHL ($n=35$) in **f**, available specimens must have had 7,500 sampled events. One patient with R/R cHL who had sufficient events for the analysis of CD3$^+$ clusters in (Fig. 3f) had <7,500 CD3$^-$ sampled events and was excluded from the CD3$^-$ analysis in **f**.

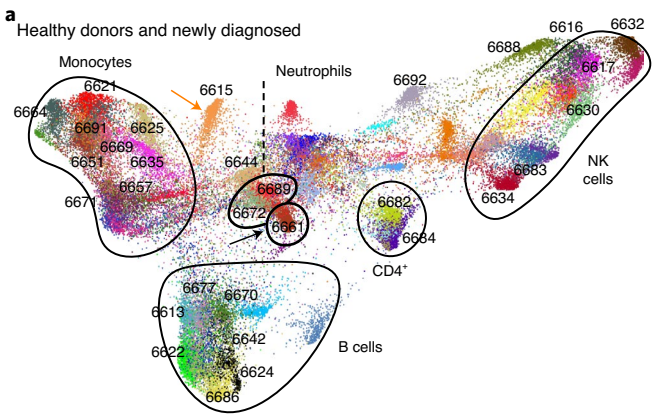

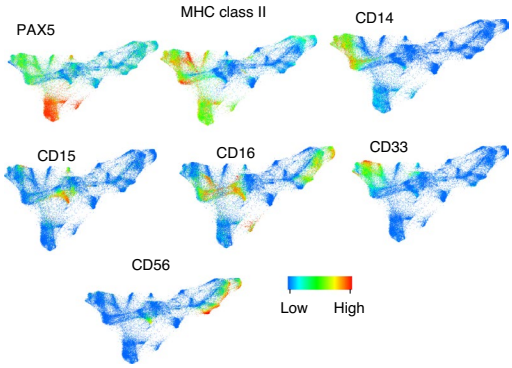

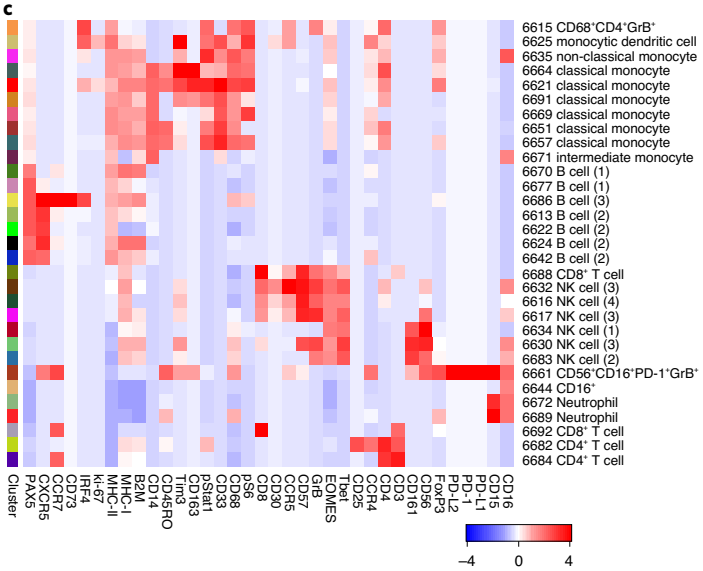

d

CD3⁻ cell subsets	
Classical monocytes	CD33⁺CD14⁺CD16⁻
Non-classical monocytes	CD33⁺CD14⁻CD16⁺
Intermediate monocytes	CD14⁺CD16⁺
Monocytic dendritic cells	CD33⁺CD14⁻CD16⁻MHC class II⁺
CD14⁺ dendritic cells	CD33⁻CD14⁺CD16⁻MHC class II⁺
B cells	PAX5⁺MHC class II⁺ 1) CXCR5⁻CD73⁻IRF4⁻ 2) CXCR5⁺CD73⁻IRF4⁻ 3) CXCR5⁺CD73⁺IRF4⁺
NK cells	CD56⁺
Neutrophils	CD15⁺CD16⁺

e

	Cluster ID nos.	NK subset
Healthy donors and newly diagnosed	6634	(1) CD56 bright
	6683	(2) CD56+/immature
	6630	(3) CD56+/mature
	6617	(3) CD56+/mature
	6632	(3) CD56+/mature
	6616	(4) Adaptive
Newly diagnosed and R/R	720	(1) CD56 bright
	725	(2) CD56+/immature
	714	(3) CD56+/mature
	735	(4) Adaptive

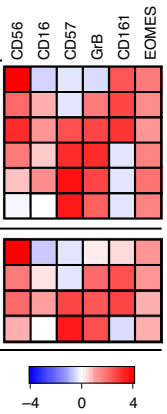

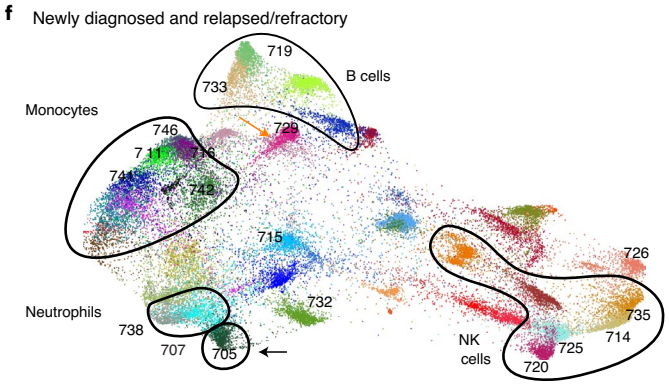

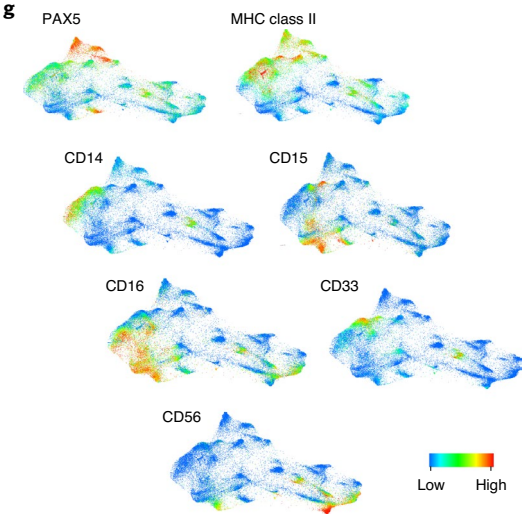

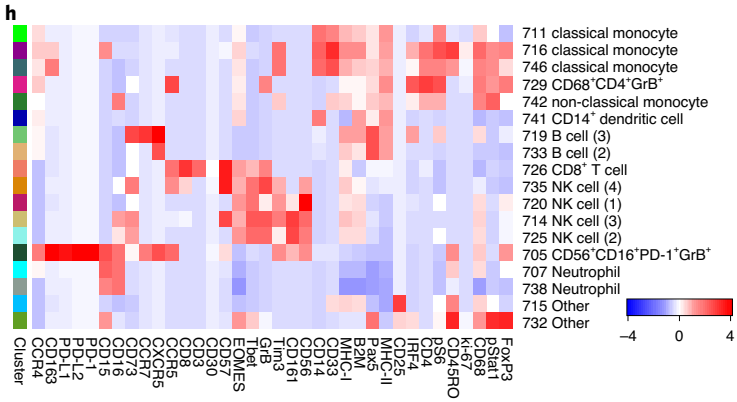

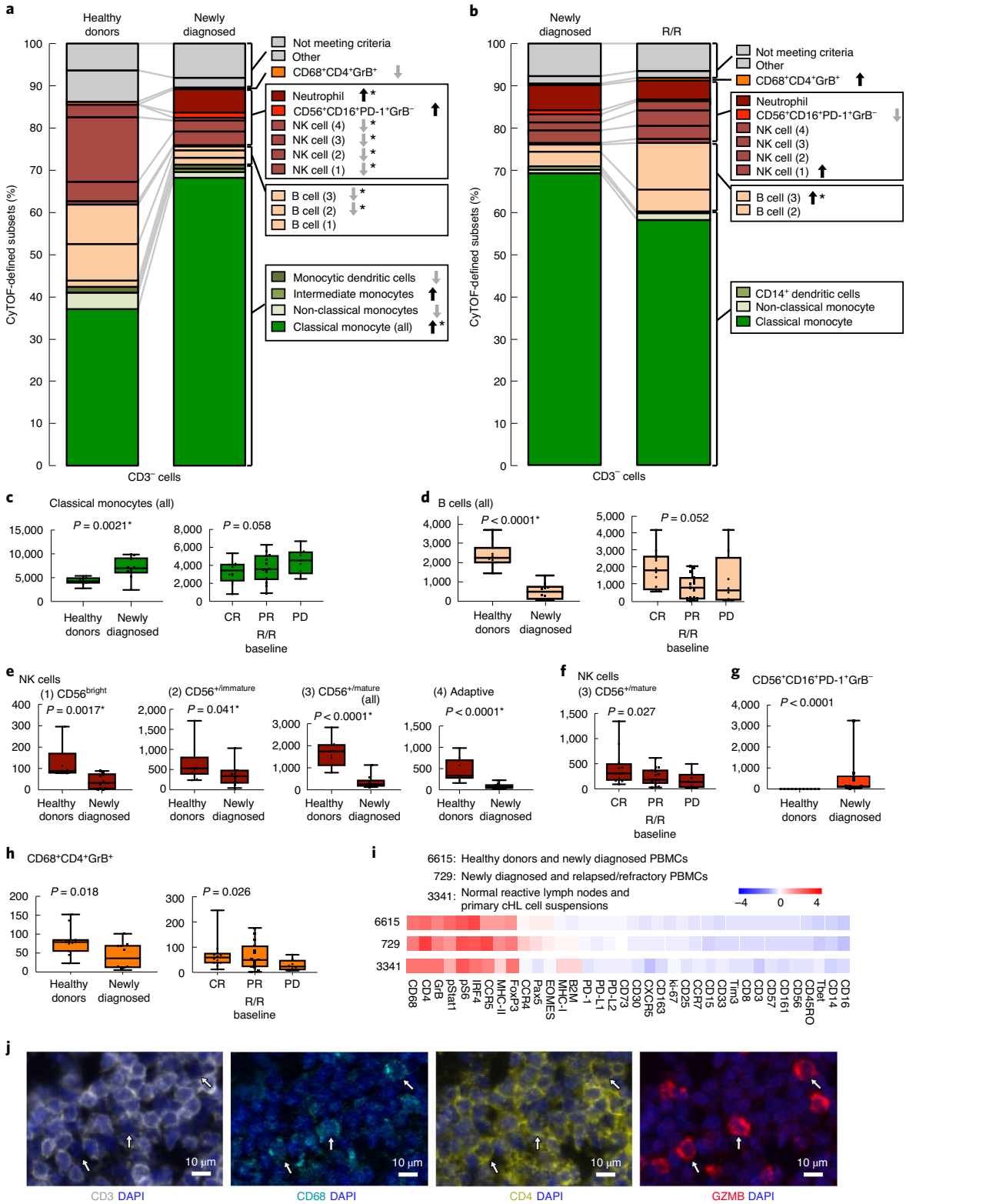

enhanced interleukin-2 and interleukin-12 signaling[56]. In certain solid tumors, NK cell abundance was associated with more favorable responses to PD-1 blockade[57].

In this study, we identified an additional circulating CD3⁻CD68⁺CD4⁺GrB⁺ subset that was associated with response to PD-1 blockade and detectable in the TME of relapsed cHLs. Human monocytes, like NK cells, may utilize granzyme B to destroy antibody-coated targets via antibody-dependent cellular cytotoxicity[58]. As circulating B cell abundance was also associated with response to PD-1 blockade in cHL, immunoglobulins directed against tumor antigens could promote antibody-dependent cellular cytotoxicity of HRS cells by innate effectors[59]. Of importance, patients with cHL with the most favorable responses to PD-1 blockade had coordinate CD3⁻ peripheral immune signatures—increased circulating B cells, NK cells and CD68⁺GrB⁺ innate cells—more like those of healthy donors.

Fig. 6 | Comparative analyses of CD3⁻ clusters in healthy donors and patients with newly diagnosed and R/R cHL. a,**b**, The differences in abundance of the CD3⁻ clusters in healthy donors versus newly diagnosed patients (**a**) and newly diagnosed patients versus those with R/R disease (**b**) are displayed in comparison bar graphs with highlighted statistically significant differences (Wilcoxon rank-sum test with nominal two-sided $P \leq 0.05$). *P* values that remained significant after Benjamini–Hochberg correction are noted (with an asterisk). See also Extended Data Figs. 6a–d, 7a–d and 8a–d for exact *P* values. **a**, Healthy donors versus newly diagnosed patients. **b**, Newly diagnosed patients versus patients with R/R cHL. **c**, Classical monocytes (all) at baseline in healthy donors versus newly diagnosed patients (left) and patients with R/R cHL by BOR (right). **d**, B cells (all) at baseline in healthy donors versus newly diagnosed patients (left) and patients with R/R cHL by BOR (right). **e**, NK cell subsets at baseline in healthy donors versus newly diagnosed patients. **f**, CD56$^{+/mature}$ NK cells at baseline in patients with R/R disease by BOR. **g**, CD56⁺CD16⁺PD-1⁺GrB⁻ subset at baseline in healthy donors versus newly diagnosed patients. **h**, CD3⁻CD68⁺CD4⁺GrB⁺ subset at baseline in healthy donors versus newly diagnosed patients (left) and patients with R/R disease (right) by BOR. Clusters with similar phenotypes, such as classical monocytes 6664, 6621, 6691, 6669, 6651 and 6657, were collapsed for these analyses. In **c**–**h**, differences between healthy and newly diagnosed groups were assessed by Wilcoxon rank-sum test, and Cuzick trend test was used to compare patients with R/R cHL by response (CRs, PRs and PDs). All tests were two-sided, and equal variance was not assumed. Given the heterogeneity in CD3⁻ cells, nominal *P* values are provided for all individual cluster comparisons. Separate Benjamini–Hochberg corrections were performed in classical monocytes, B cells or NK cell groups; nominal *P* values that retain significance are noted (with an asterisk). All box plots (generated in GraphPad Prism) define the 25th and 75th percentiles and median values, and whiskers show the minimum and maximum values. **i**, Full phenotype of the CD3⁻CD68⁺CD4⁺GrB⁺ clusters from PBMCs of healthy donors and newly diagnosed patients with cHL (ID no. 6615) and newly diagnosed patients and those with R/R disease with cHL (ID no. 729) and normal reactive lymph nodes and primary cHL cell suspensions (ID no. 3341)[31]. **j**, Multiparametric immunofluorescence of CD3, CD68, CD4 and granzyme B with DAPI counterstain in one of the four examined biopsies of relapsed cHL. In this representative field of view, white arrows denote CD3⁻CD68⁺CD4⁺GrB⁺ cells. For inclusion in the analyses of CD3⁻ clusters in healthy donors ($n=11$) and patients with newly diagnosed cHL ($n=10$) in **a**, available specimens must have had 12,000 sampled events. For inclusion in the analyses of CD3⁻ clusters in patients with newly diagnosed cHL ($n=10$) and R/R cHL ($n=35$, ((CR $n=12$, PR $n=15$, PD $n=8$)) in **b**–**h**, available specimens must have had 7,500 sampled events. One patient with newly diagnosed cHL who had sufficient numbers of CD3⁻ sampled events in **a** had insufficient numbers of CD3⁺ sampled events and was excluded from the CD3⁺ analysis (in Fig. 3a). One patient with R/R cHL had sufficient numbers of CD3⁺ sampled events for inclusion in Fig. 3f, but had insufficient numbers of CD3⁻ sampled events and was excluded from the CD3⁻ analyses in **b**–**h**.

Taken together, our studies of the peripheral immune signature in cHL revealed potential complementary roles of newly expanded, clonally diverse CD4⁺ T cells and additional innate effectors in the response to PD-1 blockade. These new insights may lead to the identification of predictive biomarkers and additional rational therapeutic targets to evaluate in concert with PD-1 blockade in cHL and other tumors.

Online content

Any methods, additional references, Nature Research reporting summaries, source data, extended data, supplementary information, acknowledgements, peer review information; details of author contributions and competing interests; and statements of data and code availability are available at https://doi.org/10.1038/s41591-020-1006-1.

Received: 21 November 2019; Accepted: 1 July 2020;
Published online: 10 August 2020

References

1. Mathas, S., Hartmann, S. & Kuppers, R. Hodgkin lymphoma: pathology and biology. *Semin. Hematol.* **53**, 139–147 (2016).
2. Green, M. R. et al. Integrative analysis reveals selective 9p24.1 amplification, increased PD-1 ligand expression, and further induction via JAK2 in nodular sclerosing Hodgkin lymphoma and primary mediastinal large B-cell lymphoma. *Blood* **116**, 3268–3277 (2010).
3. Roemer, M. G. et al. PD-L1 and PD-L2 genetic alterations define classical hodgkin lymphoma and predict outcome. *J. Clin. Oncol.* **34**, 2690–2697 (2016).
4. Roemer, M. G. M. et al. Major histocompatibility complex class II and programmed death ligand 1 expression predict outcome after programmed death 1 blockade in classic hodgkin lymphoma. *J. Clin. Oncol.* **36**, 942–950 (2018).
5. Wienand, K. et al. Genomic analyses of flow-sorted hodgkin reed-sternberg cells reveal complementary mechanisms of immune evasion. *Blood Adv.* **3**, 4065–4080 (2019).
6. Wherry, E. J. & Kurachi, M. Molecular and cellular insights into T cell exhaustion. *Nat. Rev. Immunol.* **15**, 486–499 (2015).
7. Ansell, S. M. et al. PD-1 blockade with nivolumab in relapsed or refractory Hodgkin's lymphoma. *N. Engl. J. Med.* **372**, 311–319 (2015).
8. Armand, P. et al. Nivolumab for relapsed/refractory classic hodgkin lymphoma after failure of autologous hematopoietic cell transplantation: Extended follow-up of the multicohort single-arm phase II CheckMate 205 trial. *J. Clin. Oncol.* **36**, 1428–1439 (2018).
9. Armand, P. et al. Programmed death-1 blockade with pembrolizumab in patients with classical hodgkin lymphoma after brentuximab vedotin failure. *J. Clin. Oncol.* **34**, 3733–3739 (2016).
10. Chen, R. et al. Phase II study of the efficacy and safety of pembrolizumab for relapsed/refractory classic hodgkin lymphoma. *J. Clin. Oncol.* **35**, 2125–2132 (2017).
11. Shi, Y. et al. Safety and activity of sintilimab in patients with relapsed or refractory classical Hodgkin lymphoma (ORIENT-1): a multicentre, single-arm, phase 2 trial. *Lancet Haematol.* **6**, e12–e19 (2019).
12. Song, Y. et al. Treatment of relapsed or refractory classical Hodgkin lymphoma with the anti-PD-1, tislelizumab: results of a phase 2, single-arm, multicenter study. *Leukemia* **34**, 533–542 (2020).
13. Song, Y. et al. A single-arm, multicenter, phase 2 study of camrelizumab in relapsed or refractory classical Hodgkin lymphoma. *Clin. Cancer Res.* **25**, 7363–7369 (2019).
14. Merryman, R. W., Armand, P., Wright, K. T. & Rodig, S. J. Checkpoint blockade in Hodgkin and non-Hodgkin lymphoma. *Blood Adv.* **1**, 2643–2654 (2017).
15. Ramchandren, R. et al. Nivolumab for newly diagnosed advanced-stage classic hodgkin lymphoma: safety and efficacy in the phase II CheckMate 205 study. *J. Clin. Oncol.* **37**, 1997–2007 (2019).
16. Tumeh, P. C. et al. PD-1 blockade induces responses by inhibiting adaptive immune resistance. *Nature* **515**, 568–571 (2014).
17. Im, S. J. et al. Defining CD8⁺ T cells that provide the proliferative burst after PD-1 therapy. *Nature* **537**, 417–421 (2016).
18. Kamphorst, A. O. et al. Rescue of exhausted CD8 T cells by PD-1-targeted therapies is CD28-dependent. *Science* **355**, 1423–1427 (2017).
19. Juneja, V. R. et al. PD-L1 on tumor cells is sufficient for immune evasion in immunogenic tumors and inhibits CD8 T cell cytotoxicity. *J. Exp. Med.* **214**, 895–904 (2017).
20. Reichel, J. et al. Flow sorting and exome sequencing reveal the oncogenome of primary Hodgkin and Reed–Sternberg cells. *Blood* **125**, 1061–1072 (2015).
21. Roemer, M. G. et al. Classical hodgkin lymphoma with reduced β2M/MHC class I expression is associated with inferior outcome independent of 9p24.1 status. *Cancer Immunol. Res.* **4**, 910–916 (2016).
22. Johnson, D. B. et al. Melanoma-specific MHC-II expression represents a tumour-autonomous phenotype and predicts response to anti-PD-1/PD-L1 therapy. *Nat. Commun.* **7**, 10582 (2016).
23. Kreiter, S. et al. Mutant MHC class II epitopes drive therapeutic immune responses to cancer. *Nature* **520**, 692–696 (2015).
24. Linnemann, C. et al. High-throughput epitope discovery reveals frequent recognition of neo-antigens by CD4⁺ T cells in human melanoma. *Nat. Med.* **21**, 81–85 (2015).
25. Ott, P. A. et al. An immunogenic personal neoantigen vaccine for patients with melanoma. *Nature* **547**, 217–221 (2017).

26. Choi, I. K. et al. Signaling by the Epstein–Barr virus LMP1 protein induces potent cytotoxic CD4$^+$ and CD8$^+$ T cell responses. *Proc. Natl Acad. Sci. USA* **115**, E686–E695 (2018).
27. Alspach, E. et al. MHC-II neoantigens shape tumour immunity and response to immunotherapy. *Nature* **574**, 696–701 (2019).
28. Kanzler, H., Kuppers, R., Hansmann, M. L. & Rajewsky, K. Hodgkin and Reed–Sternberg cells in Hodgkin's disease represent the outgrowth of a dominant tumor clone derived from (crippled) germinal center B cells. *J. Exp. Med.* **184**, 1495–1505 (1996).
29. Weniger, M. A. et al. Human CD30$^+$ B cells represent a unique subset related to Hodgkin lymphoma cells. *J. Clin. Invest.* **128**, 2996–3007 (2018).
30. Carey, C. D. et al. Topological analysis reveals a PD-L1-associated microenvironmental niche for Reed–Sternberg cells in Hodgkin lymphoma. *Blood* **130**, 2420–2430 (2017).
31. Cader, F. Z. et al. Mass cytometry of Hodgkin lymphoma reveals a CD4$^+$ regulatory T-cell-rich and exhausted T-effector microenvironment. *Blood* **132**, 825–836 (2018).
32. Bakhru, P. et al. Combination central tolerance and peripheral checkpoint blockade unleashes antimelanoma immunity. *JCI Insight* **2**, e93265 (2017).
33. Hogan, S. A. et al. Peripheral blood TCR repertoire profiling may facilitate patient stratification for immunotherapy against melanoma. *Cancer Immunol. Res.* **7**, 77–85 (2019).
34. Jacquelot, N. et al. Predictors of responses to immune checkpoint blockade in advanced melanoma. *Nat. Commun.* **8**, 592 (2017).
35. Krieg, C. et al. High-dimensional single-cell analysis predicts response to anti-PD-1 immunotherapy. *Nat. Med.* **24**, 144–153 (2018).
36. Manjarrez-Orduno, N. et al. Circulating T cell subpopulations correlate with immune responses at the tumor site and clinical response to PD1 inhibition in non-small cell lung cancer. *Front Immunol.* **9**, 1613 (2018).
37. Spitzer, M. H. et al. Systemic immunity is required for effective cancer immunotherapy. *Cell* **168**, 487–502 (2017).
38. Zuazo, M. et al. Functional systemic CD4 immunity is required for clinical responses to PD-L1/PD-1 blockade therapy. *EMBO Mol. Med* **11**, e10293 (2019).
39. Mackall, C. L. T-cell immunodeficiency following cytotoxic antineoplastic therapy: a review. *Stem Cells* **18**, 10–18 (2000).
40. Glowala-Kosinska, M. et al. Thymic activity and T cell repertoire recovery after autologous hematopoietic stem cell transplantation preceded by myeloablative radiotherapy or chemotherapy. *Biol. Blood Marrow Transpl.* **22**, 834–842 (2016).
41. Ljungman, P. et al. Vaccination of hematopoietic cell transplant recipients. *Bone Marrow Transpl.* **44**, 521–526 (2009).
42. Samusik, N., Good, Z., Spitzer, M. H., Davis, K. L. & Nolan, G. P. Automated mapping of phenotype space with single-cell data. *Nat. Methods* **13**, 493–496 (2016).
43. Godfrey, D. I., Koay, H. F., McCluskey, J. & Gherardin, N. A. The biology and functional importance of MAIT cells. *Nat. Immunol.* **20**, 1110–1128 (2019).
44. Pillay, J., Tak, T., Kamp, V. M. & Koenderman, L. Immune suppression by neutrophils and granulocytic myeloid-derived suppressor cells: similarities and differences. *Cell. Mol. Life Sci.* **70**, 3813–3827 (2013).
45. Freud, A. G., Mundy-Bosse, B. L., Yu, J. & Caligiuri, M. A. The broad spectrum of human natural killer cell diversity. *Immunity* **47**, 820–833 (2017).
46. Vari, F. et al. Immune evasion via PD-1/PD-L1 on NK cells and monocyte/macrophages is more prominent in Hodgkin lymphoma than DLBCL. *Blood* **131**, 1809–1819 (2018).
47. Pauken, K. E. et al. Epigenetic stability of exhausted T cells limits durability of reinvigoration by PD-1 blockade. *Science* **354**, 1160–1165 (2016).
48. Sen, D. R. et al. The epigenetic landscape of T cell exhaustion. *Science* **354**, 1165–1169 (2016).
49. Kurtulus, S. et al. Checkpoint blockade immunotherapy induces dynamic changes in PD-1$^-$CD8$^+$ tumor-infiltrating T cells. *Immunity* **50**, 181–194 e186 (2019).
50. Siddiqui, I. et al. Intratumoral Tcf1$^+$PD-1$^+$CD8$^+$ T cells with stem-like properties promote tumor control in response to vaccination and checkpoint blockade immunotherapy. *Immunity* **50**, 195–211 e110 (2019).
51. Miller, B. C. et al. Subsets of exhausted CD8$^+$ T cells differentially mediate tumor control and respond to checkpoint blockade. *Nat. Immunol.* **20**, 326–336 (2019).
52. Sade-Feldman, M. et al. Defining T cell states associated with response to checkpoint immunotherapy in melanoma. *Cell* **175**, 998–1013 e1020 (2018).
53. Acharya, N. & Anderson, A. C. New clones on the block. *Immunity* **51**, 606–608 (2019).
54. Yost, K. E. et al. Clonal replacement of tumor-specific T cells following PD-1 blockade. *Nat. Med.* **25**, 1251–1259 (2019).
55. Perez-Diez, A. et al. CD4 cells can be more efficient at tumor rejection than CD8 cells. *Blood* **109**, 5346–5354 (2007).
56. Porichis, F. et al. Immune checkpoint blockade restores HIV-specific CD4 T cell help for NK cells. *J. Immunol.* **201**, 971–981 (2018).
57. Barry, K. C. et al. A natural killer-dendritic cell axis defines checkpoint therapy-responsive tumor microenvironments. *Nat. Med.* **24**, 1178–1191 (2018).
58. Elavazhagan, S. et al. Granzyme B expression is enhanced in human monocytes by TLR8 agonists and contributes to antibody-dependent cellular cytotoxicity. *J. Immunol.* **194**, 2786–2795 (2015).
59. Hu, X. et al. Landscape of B cell immunity and related immune evasion in human cancers. *Nat. Genet.* **51**, 560–567 (2019).

Methods

Patient samples. Baseline and on-treatment cryopreserved PBMCs were obtained from patients with relapsed/refractory R/R cHL who received single-agent nivolumab in a multicenter, multicohort phase II trial, CheckMate 205 (ClinicalTrials.gov identifier: NCT02181738)[8] and gave written informed consent. The institutional review board at each institution participating in the CheckMate 205 clinical trials[8] approved the banking of PBMC samples for associated research studies. The Dana-Farber Cancer Institute IRB also approved the laboratory research studies. CheckMate 205 included patients with R/R cHL who previously underwent ASCT and received: no brentuximab vedotin (BV) (Cohort A); BV after ASCT (Cohort B); or BV before and/or after ASCT (Cohort C). Patients were treated with nivolumab (3 mg per kg (body weight)) every 2 weeks until disease progression or unacceptable toxicity. BOR was assessed by an independent review committee using 2007 International Working Group response criteria[8]. Cryopreserved PBMCs were also obtained from: (1) patients with newly diagnosed, previously untreated cHL, with informed consent; and (2) normal healthy donors (Supplementary Table 1). Samples from normal healthy donors were obtained under an umbrella protocol for otherwise discarded anonymized tissues.

Peripheral blood samples were collected in 8-ml Vacutainer Cell Preparation Tubes, and PBMCs were isolated by centrifugation and cryopreserved for subsequent TCR sequencing and CyTOF analysis.

CD4⁺ and CD8⁺ cell separation of PBMCs. In cases with an additional available PBMC sample, purified unmanipulated CD4⁺ and CD8⁺ cells were obtained from the bulk PBMCs by negative selection using Miltenyi Biotec separation kits: CD4⁺ T cell isolation (includes CD8, CD14, CD15, CD16, CD19, CD36, CD56, CD123, TCR gamma/delta and CD235a biotin-conjugated monoclonal antibodies, no. 130-096-533) and CD8⁺ T cell isolation (includes CD4, CD14, CD15, CD16, CD19, CD36, CD56, CD123, TCR gamma/delta and CD235a biotin-conjugated monoclonal antibodies, no. 130-096-495). Cryopreserved cells were partially thawed and resuspended in warmed RPMI medium supplemented with FBS (1:1 vol/vol). To remove large clumps and ensure a single-cell suspension, cells were passed through a 70-µm cell strainer. The cell suspension was split into 2 tubes, (a) and (b), and washed by centrifugation (300*g*, 5 min). The supernatants were aspirated and pellets were resuspended in 40 µl of cold Miltenyi buffer (1:20 BSA stock (no. 130-091-376) diluted with AutoMACS rinsing solution (no. 130-091-222)). Ten microliters of CD4⁺ negative selection, biotin-conjugated antibody cocktail or CD8⁺ negative selection, biotin-conjugated antibody cocktail was added to the cell suspension (tube (a) or (b), respectively). Samples were mixed well and refrigerated for 5 min. Next, 30 µl of Miltenyi buffer was added followed by 20 µl of the appropriate microbeads (tube (a) or (b), respectively). Samples were again mixed well and refrigerated for 10 min.

Isolation of highly purified CD4⁺ or CD8⁺ T cells was achieved by depletion of magnetically labeled cells. Specifically, LS columns (Miltenyi Biotec no. 130-042-401) were placed in a quadroMACS separator magnet (Miltenyi Biotec) and rinsed with 3 ml of Miltenyi buffer. Each cell suspension was supplemented to 500 µl and added to a rinsed column (1 column per sample), and flow through was collected into a new tube. The column was then washed with 3 ml of buffer and combined with cell suspension effluent.

T cell receptor sequencing and repertoire analysis. Genomic DNA was extracted from unsorted bulk PBMC samples and the negatively selected CD4⁺ (CD8⁺-depleted) and CD8⁺ (CD4⁺-depleted) cell subsets using the commercially available Qiagen DNAeasy kit no. 69506 and subsequently subjected to T cell receptor (TCR) sequencing. TCR beta chain CDR3 regions were sequenced by ImmunoSeq (Adaptive Biotechnologies), using multiplex PCR with primers annealing to V and J segments, resulting in amplification of rearranged VDJ segments from each cell. By comparing to a synthetic immune receptor repertoire, amplification biases were identified and minimized, and residual bias were computationally removed after sequencing[60]. A list of TCR sequences and their copy numbers/counts ($c \in \mathbb{N}^m_{\geq 0}$) was then generated, where m is the sequence numbers and $\mathbb{N}^m_{\geq 0}$ is a set of non-negative integers with the size of m.

TCR-seq results were analyzed by custom Python scripts, which compute the Shannon entropy index (H) for repertoire diversity, reflecting both richness and evenness of the repertoire[61]. For any repertoire $c \in \mathbb{N}^m_{\geq 0}$, where c_i is the count of sequence i and $\sum_j c_j$ is the summation of all sequence counts, we defined the Shannon entropy diversity index by

$$H(c) = -\sum_i \frac{c_i}{\sum_j c_j} \log_2 \left(\frac{c_i}{\sum_j c_j} \right)$$

Unsorted T cells and sorted CD4⁺ and CD8⁺ T cells were analyzed separately, except where 'CD4⁺ and CD8⁺' analyses are indicated in the manuscript. For 'CD4⁺ and CD8⁺' analyses, the CD4⁺ and CD8⁺ TCR sequences were combined in silico. The changes in TCR repertoire diversity over time were measured from C1D1 (baseline) to C4D1 and evaluated in paired samples using Wilcoxon tests. For a subset of nine trial patients with previously determined HRS cell expression of MHC class I and II[4], changes in TCR diversity were separately evaluated according to HRS MHC class I and II status.

Clonal expansion following PD-1 blockade. To measure the level of clonal expansion after immunotherapy, we computed the fold change of the clonal frequency before (C1D1) and after the treatment (C2D1 and C4D1). For every clone in each patient, we defined the clonal expansion level $E = max\left(\frac{f_{C2D1}}{f_{C1D1}}, \frac{f_{C4D1}}{f_{C1D1}}\right)$, where f was the clonal frequency in each repertoire for clones of the same TCR beta chain protein sequence. If a clone could not be detected in the sample prior to treatment (C1D1) but was observed at C2D1 or C4D1, we added a pseudocount 0.5 at C1D1 to avoid division by 0. We defined a twofold ($E \geq 2$) increase at any timepoint after treatment in a given clonotype as T cell expansion. Singleton clones were defined as having zero or one copy at C1D1 whereas non-singleton clones had two or more copies at C1D1.

Clonal expansion was first evaluated by tracing clones of the same protein sequence in unsorted T cells. Next, using data from the sorted CD4⁺ and CD8⁺ T cells, we annotated the origin of expanded clones as CD4⁺, CD8⁺ or unknown depending on the presence of the same protein sequence in sorted T cells of the same patient. The same computational procedure was applied to all clones in the unsorted T cell samples, allowing estimation of the relative proportion of expanded CD4⁺ or CD8⁺ T cells over the specific population in Extended Data Fig. 1k,l and Fig. 2g.

Antibodies. Mass-cytometry antibodies and reporter isotopes are included in Supplementary Table 2 and described in Cader et al.[31].

CyTOF sample preparation. Samples were prepared and stained as previously described[31]. In brief, individual samples were rapidly thawed and assayed for viability[31]. Thereafter, cells were washed, resuspended in cell-staining medium and incubated with human FcR blocking reagent and, subsequently, the surface antibody cocktail[31]. After washing and permeabilization, samples were incubated with the intracellular antibody cocktail, washed and treated with the DNA intercalator, as described[31]. After additional washes, cells were resuspended at a concentration of 1×10^6 cells ml^{-1} in deionized water containing calibration beads[31].

Mass cytometry data analysis. CyTOF data acquisition is described in detail in Cader et al.[31]. CyTOF analyses of trial patient samples were performed blinded to clinical parameters.

Analyses of T cell differentiation. Using the Cytobank platform, we first manually gated the CyTOF data from cHL trial patients to identify viable, singlet cells and then all CD3⁺ cells, CD3⁺CD4⁺ and CD3⁺CD8⁺ T cell subsets. CD4⁺CD8⁺ and CD4⁻CD8⁻ cells were excluded. Thereafter, all T cells, CD4⁺ T cells and CD8⁺ T cells were evaluated for differentiation status on the basis of CCR7 and CD45RO expression: naive (CCR7⁺CD45RO⁻), CM (CCR7⁺CD45RO⁺), EM (CCR7⁻CD45RO⁺) or TEMRA (CCR7⁻CD45RO⁻).

VorteX clustering and visualization. The Cytobank platform was used for bead-based normalization, identification of viable singlets and selection of relevant populations to export[31]. An equivalent number of single cells from each sample were imported into the VorteX visualization environment and clustered with the algorithm, X-shift (version 'VorteX 26-Apr-2018') as previously described[31,42]. Seven separate X-shift analyses were performed: (1) CD3⁺ cells and (2) CD3⁻ cells from healthy donors and patients with newly diagnosed cHL, sampling 12,000 events; (3) CD3⁺ cells and (4) CD3⁻ cells from patients with newly diagnosed and R/R cHL, sampling 7,500 events and (5) CD3⁺ cells and (6) CD3⁻ cells from all cases, sampling 7,500 events. Lastly, (7) CD3⁻ cells from a previous CyTOF analysis of normal reactive lymph nodes and primary cHL suspensions[31] were reanalyzed, sampling 4,500 events on the basis of available cell counts from the smallest specimen.

For analyses (3) and (4), only patients with R/R cHL who initiated PD-1 blockade ≥12 months from completion of ASCT were included. Data interpretation for analyses (5) and (6) was restricted to patients with an interval of ≥12 months between their prior myeloablative ASCT and study therapy (nivolumab) who had paired Cycle 1 Day 1 (C1D1) and Cycle 4 Day 1 (C4D1) samples.

For the CD3⁻ cell analysis, all antibody channels were used to perform the clustering in the viable singlet population. For the CD3⁺ cell analysis, all antibody channels except PAX5, CD163, CD14, CD33 and CD68 were used.

Force-directed layouts and heatmaps. After X-shift analysis, a randomly sampled proportional number of events from each sample were visualized in a force-directed layout (FDL), in which similar clusters were more closely aligned in two-dimensional space as previously described[31]. Each cluster was assigned a unique color with hex color code software (http://www.color-hex.com). The protein-expression profiles of each cluster were visualized in a heatmap as previously described[31]. In brief, median protein expression levels were collated in an overall expression matrix which was then normalized into *Z*-scores (−4 to +4) in R (scale function) and bidirectionally clustered using 'pheatmap' package[31]. Clusters were phenotypically labeled using known lineage, differentiation and polarization markers[31]. We applied an inclusion criteria of at least 100 events in each cluster in a minimum of 10% of samples.

To quantify the immune clusters in healthy donors, patients with newly diagnosed cHL and patients with R/R cHL at baseline, we calculated the median cluster cell counts in each group. We further subdivided patients with R/R cHL at baseline and C4D1 according to BOR to nivolumab therapy.

Comparative analysis of PD-1 expression. In each analyzed sample, PD-1 expression was calculated as the median PD-1 level for all cells in the associated VorteX cluster. *Z*-score-normalized PD-1 expression values for each $CD3^+$ cluster were determined and included in Fig. 4. From the analysis in Fig. 4b, T cell subsets from patients with newly diagnosed or R/R cHL were separately evaluated for PD-1 expression (Extended Data Fig. 4d). The differences in PD-1 expression in T cell subsets from newly diagnosed patients and those with R/R cHL were measured by the Wilcoxon rank-sum test with two-sided *P* values.

Statistical Methods. In TCR-seq analyses, we reported two-sided *P* values for bulk T cell analyses and one-sided *P* values for $CD4^+$ and $CD8^+$ T cell analyses as the bulk data provided directions for the subsequent $CD4^+$ and $CD8^+$ comparisons.

Distributions for each CyTOF-defined cluster in $CD3^+$ and $CD3^-$ populations were represented as median and IQR with individual data points displayed. In patients with cHL, associations with disease status (newly diagnosed, R/R) and response groups (CR > PR > PD) were assessed with a Wilcoxon rank-sum test or a Cuzick trend test[62] for ordinal response categories. Nominal *P* values were reported for exploratory or supplemental analyses; *P* values < 0.05 were considered statistically significant. A Benjamini–Hochberg correction[63] was used to control the false-discovery rate in $CD3^+$ ($CD4^+$ and $CD8^+$) cell types. Given the heterogeneity in $CD3^-$ cells, we have provided nominal *P* values for all individual cluster comparisons. Separate Benjamini–Hochberg corrections were performed to control for false-discovery rate within classical monocytes, B cells or NK cell groups. Statistical analyses were performed using R (version 3.3.2). All tests were two-sided and equal variance was not assumed.

Immunohistochemical analyses of formalin-fixed paraffin-embedded samples. *Sample acquisition.* Additional formalin-fixed, paraffin-embedded (FFPE) lymph-node biopsies from patients with cHL who relapsed following ABVD induction therapy were obtained from the archives of Brigham & Women's Hospital, Boston, MA, with approval from the institutional review board (2014P001721). H&E-stained tissue sections and the original diagnostic reports were reviewed by an expert hematopathologist (S.J.R.).

Multiplex immunofluorescence. Multiplex immunofluorescence staining and analysis was performed as previously described on a Bond RX autostainer[30,64]. Five-micrometer-thick FFPE tissue sections were deparaffinized (Bond DeWax, Leica Biosystems) and rehydrated per standard protocols. Antigen retrieval was performed (ER1, Leica Biosystems) at pH 6 for 10 min at 98 °C. Slides were next serially stained with antibodies (40 min per antibody). Anti-rabbit polymeric horseradish peroxidase (poly-HRP, BOND Polymer Refine Detection Kit, Leica Biosystems) was then applied for 10 min. Signals for antibody complexes were then labeled and visualized with corresponding Opal Fluorophore Reagents (5-min incubation). The same process was repeated for subsequent antibodies and fluorescent dyes. Finally, Prolong Diamond Anti-fade mounting medium (no. P36965, Life Technologies) was applied, and the stained slides were stored in a light-proof box at 4 °C before imaging.

The target antigens, antibody clones and dilutions for markers used in this analysis are included in Supplementary Table 3.

Image acquisition and cell identification. Image acquisition was performed using the Mantra multispectral imaging platform (PerkinElmer). Areas with non-tumor or residual normal tissue were excluded from the analysis. Representative regions of interest were chosen by the pathologist (S.J.R.), and 3–5 fields of view were acquired at 20× resolution as multispectral images. After image capture, the fields of view were spectrally unmixed and then analyzed using supervised machine-learning algorithms within Inform 2.4 (PerkinElmer). Thresholds for positive staining and the accuracy of phenotypic algorithms were optimized and confirmed for each case.

Reporting Summary. Further information on research design is available in the Nature Research Reporting Summary linked to this article.

Data availability

The TCR sequences for this study were processed through the immunoSEQ platform of Adaptive Biotechnologies. The TCR sequences are publicly available (https://doi.org/10.21417/FZC2020NM) through this link: https://adaptivebiotech.com/pub/cader-2020-nm. The raw CyTOF.fcs files are publicly available through login at Cytobank, https://premium.cytobank.org/cytobank/experiments#project-id=2539 and https://premium.cytobank.org/cytobank/experiments/310927. Source data for all main and Extended Data figures are available in the Supplementary Dataset.

Code availability

CyTOF data was processed by VorteX (26 April 2018) and the output was processed by a custom R script. TCR-seq data was processed and analyzed by custom Python and R scripts. The code is available at https://github.com/huxihao/cHL-PBMC.

References

60. Carlson, C. S. et al. Using synthetic templates to design an unbiased multiplex PCR assay. *Nat. Commun.* **4**, 2680 (2013).
61. Rempala, G. A. & Seweryn, M. Methods for diversity and overlap analysis in T-cell receptor populations. *J. Math. Biol.* **67**, 1339–1368 (2013).
62. Cuzick, J. A Wilcoxon-type test for trend. *Stat. Med.* **4**, 87–90 (1985).
63. Benjamini, Y. & Hochberg, Y. Controlling the false discovery rate: a practical and powerful approach to multiple testing. *J. R. Stat. Soc.* **57**, 289–300 (1995).
64. Keskin, D. B. et al. Neoantigen vaccine generates intratumoral T cell responses in phase Ib glioblastoma trial. *Nature* **565**, 234–239 (2019).

Acknowledgements

This work was supported in part by Bloodwise Fellowship 14042 and a Helen Gurley Brown Fellowship (F.Z.C.), a R01 CA161026 (M.A.S.), the Miller Family Fund (M.A.S.), the BMS International Immuno-Oncology Network (M.A.S. and S.J.R.) and a R01 CA234018 (X.S.L.). The authors thank L. Boyne (Dana-Farber Cancer Institute) for providing editorial assistance.

Author Contributions

F.Z.C., X.H., X.S.L. and M.A.S. conceived and led the project and analyzed the data. F.Z.C., X.H., W.L.G., J.O., E.M., R.R., P.-H.C., J.L.W., R.C.J.S. and S.J.R. performed experiments and analyzed the data. K.W., L.N.L. B.L., W.M., P.A. and D.N. contributed to the analysis and scientific discussions. F.Z.C., X.H., X.S.L. and M.A.S. wrote the paper.

Competing interests

After completing the current studies at DFCI, F.Z.C. and X.H. became full-time employees at Astra Zeneca and GV20, respectively. P.A. consults for Merck, Bristol Myers Squibb (BMS), Pfizer, Affimed, Adaptive, Infinity, ADC Therapeutics and Celgene and receives institutional research funding from Merck, BMS, Affimed, Adaptive, Roche, Tensha, Otsuka, Sigma Tau, Genentech and IGM and honoraria from Merck and BMS. S.J.R. has received research funding from BMS, Merck, Affimed and Kite/Gilead. X.S.L. is a cofounder and board member of GV20 Oncotherapy, SAB of 3DMedCare, consultant for Genentech, and stockholder of BMY, TMO, WBA, ABT, ABBV, and JNJ. X.S.L. has received funding from Takeda and Sanofi. M.A.S. has received research funding from BMS, Merck and Bayer and has served on advisory boards for BMS and Celgene. The remaining authors declare no competing financial interests.

Additional information

Extended data is available for this paper at https://doi.org/10.1038/s41591-020-1006-1.

Supplementary information is available for this paper at https://doi.org/10.1038/s41591-020-1006-1.

Correspondence and requests for materials should be addressed to X.S.L. or M.A.S.

Peer review information Saheli Sadanand was the primary editor on this article and managed its editorial process and peer review in collaboration with the rest of the editorial team.

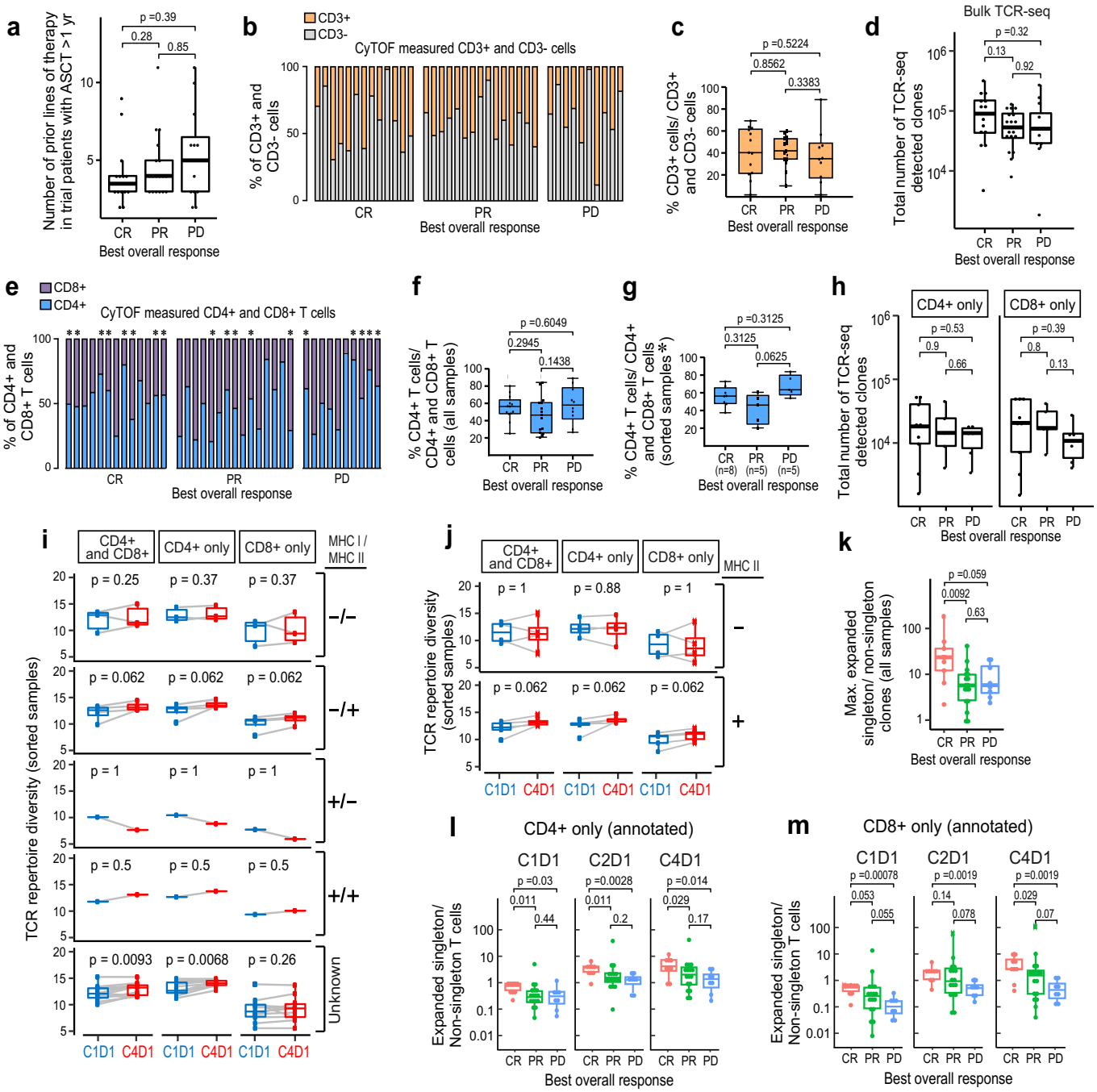

Extended Data Fig. 1 | See next page for caption.

Extended Data Fig. 1 | Analyses of peripheral TCR repertoire diversity at baseline and following PD-1 blockade. a, Number of prior therapies in trial patients who were treated with nivolumab ≥ 1 yr after ASCT by best overall response to PD-1 blockade (CR n = 14, PR n = 18, PD n = 12). **b**, Percentages of CD3 + and CD3- viable cells at baseline in trial patients with relapsed/refractory cHL. Viable singlet cells identified by manual gating of CyTOF data were divided according to CD3 expression (CD3-, grey and CD3 +, orange, n = 38). Individual samples from patients with available CyTOF files who had relapsed/refractory cHL with ≥ 1 year between nivolumab and prior myeloablative ASCT are shown (n = 38) (CR n = 13, PR n = 15, PD n = 10). **c**, Comparison of baseline CD3 + populations in trial patients with relapsed/refractory cHL (from b) according to their subsequent response to PD-1 blockade. **d**, Total number of TCR-seq detected clones at baseline in trial patients (from a) according to their subsequent response to PD-1 blockade. **e**, Percentages of CD4 + (blue) and CD8 + (purple) cells at baseline in trial patients with relapsed/refractory cHL. CD3 + cells identified (from b) and divided according to CD4 + or CD8 + expression by manual gating of CyTOF data. Additional cryopreserved samples from indicated cases (*) were available for CD4 + and CD8 + sorting (n = 18, 2 excluded from this analysis as no CyTOF files available). **f**, Comparison of baseline CD4 + populations in all trial patients with relapsed/ refractory cHL (from e) according to their subsequent response to PD-1 blockade (CR, PR, PD). **g**, Comparison of baseline CD4 + populations in trial patients with relapsed/refractory cHL (from e*) with additional PBMC samples sorted for CD4 + and CD8 + T cells (n = 18). **h**, Total numbers of CD4 + and CD8 + TCR-seq detected clones at baseline in trial patients (from g) according to their subsequent response to PD-1 blockade. Differences between groups in panels **a**, **c**, **d**, **f**, **g** and **h** were assessed with a Wilcoxon rank sum test of the median with two-tailed p values. **i**, Changes in TCR diversity from C1D1 to C4D1 in the subset of trial patients with known HRS cell expression of MHC class I and MHC class II and CD4 + and CD8 + TCRseq data (n = 9). Definitions of positive (positive or decreased) and negative expression of MHC class I and class II on HRS cells previously described in (Roemer et al 2018[4]). **j**, Changes in TCR diversity from C1D1 to C4D1 separated by HRS cell expression of MHC class II only, samples from **i**. Differences in panels i and j were assessed by Wilcoxon rank sum test with one-sided p-values. **k**, The ratio of maximum expansion of singleton clones (0 or 1 copy at baseline)/ non-singleton clones which have 2 or more copies at baseline in patients with BOR of CR (n = 9), PR (n = 17) or PD (n = 8) to PD-1 blockade. Only patients with all 3 timepoints are included in the analysis. Differences between groups were assessed with a Wilcoxon rank sum test of the median, two-tailed p values. (**l** and **m**) The ratio of expanded singleton / non-singleton clones from CD4 + only T cells (**l**) or CD8 + only T cells (**m**) from patients with CR, PR or PD to PD-1 blockade (n = 20). Differences in panels l and m were assessed by Wilcoxon rank sum test with one-sided p-values. Graphpad Prism (v8) or R (ggplot function) was used to generate box plots (GraphPad Prism panels **b**, **c**, **e-g** and **R** panels **a**, **d**, **h-m**). The box corresponds to the first and third quartiles and whiskers define minimum and maximum values. Outliers beyond 1.5x IQR in R- generated plots are plotted individually.

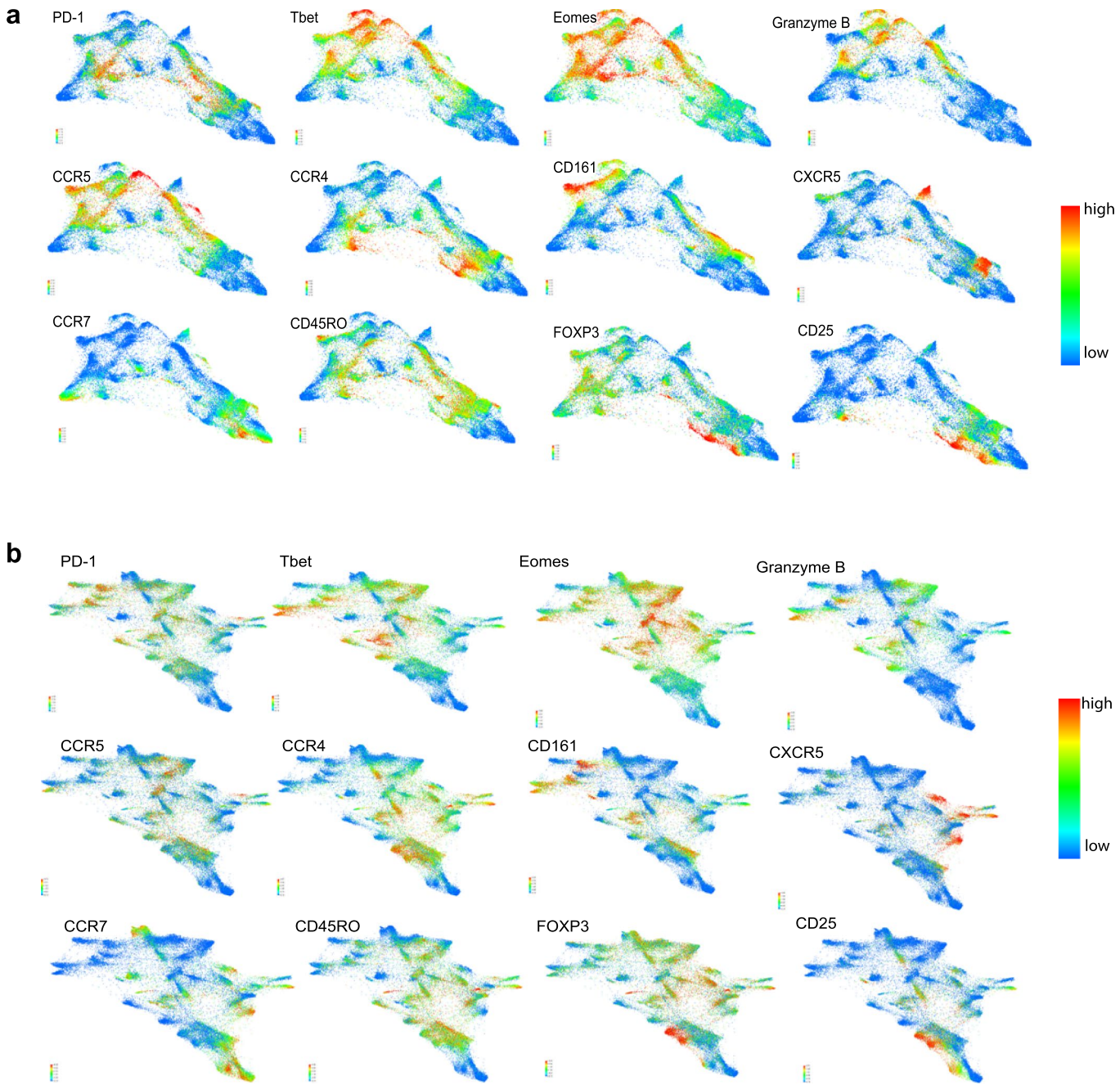

Extended Data Fig. 2 | Forced-directed layout of CD3+ populations at baseline in **a**) healthy donors and patients with newly diagnosed cHL and **b**) patients with newly diagnosed and relapsed/refractory cHL. Each FDL shows expression of individual proteins ranging from no/low expression in blue to high expression in red. Clusters can be assigned a phenotype on the basis of these FDLs. Shown here are 12 proteins which allow identification of differentiation status (CCR7, CD45RO), polarization (CCR5, CCR4, CD161), activation (PD-1, T-bet, Eomes, Granzyme B), Tregs (FoxP3, CD25) and CXCR5 + cells.

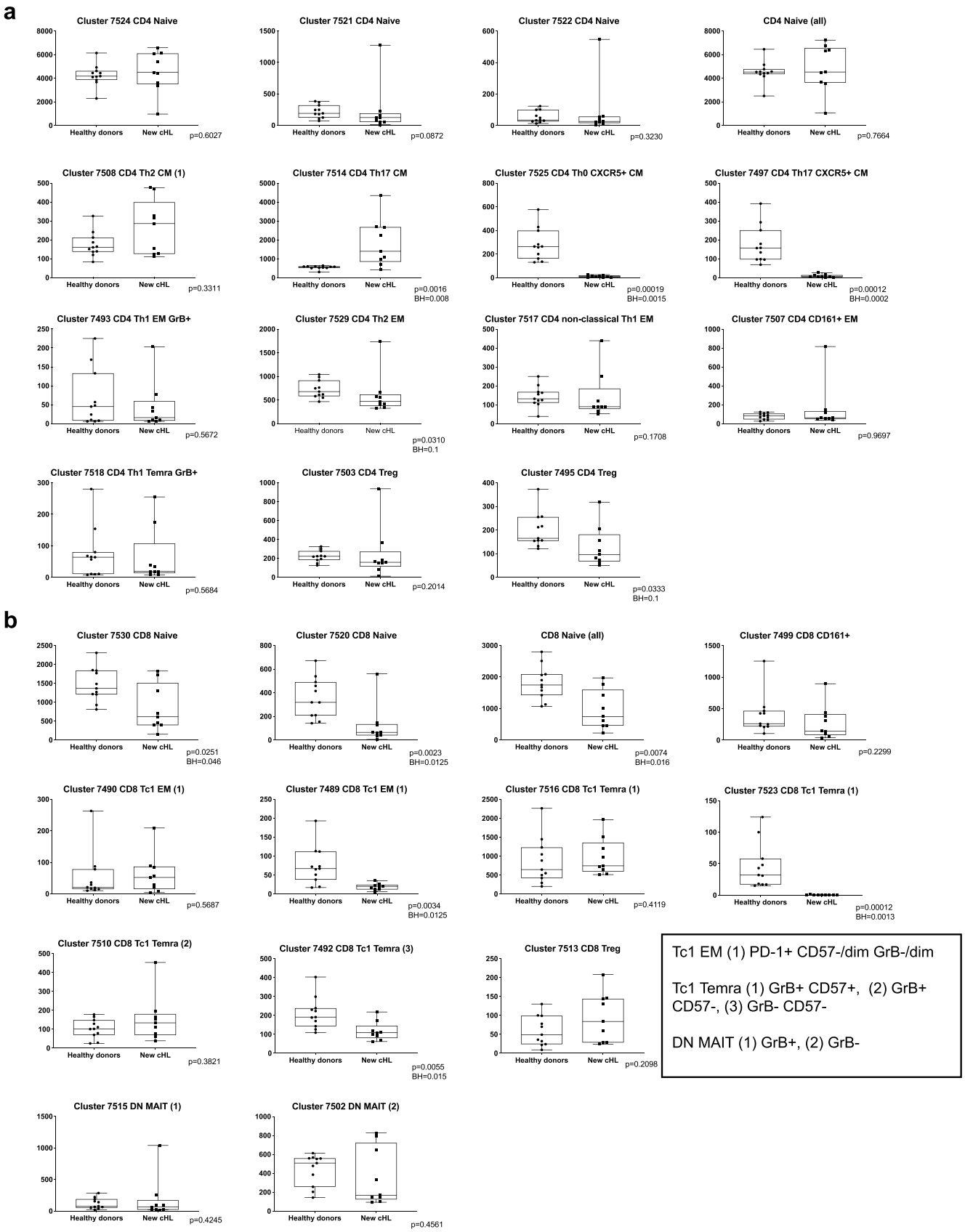

Extended Data Fig. 3 | Comparison of CD3+ populations in healthy donors versus patients with newly diagnosed cHL. To quantify differences between these 2 groups, healthy donors (n = 11) and patients with newly diagnosed cHL (n = 9), we determined the number of cells that each sample contributed to a given cluster and applied a Wilcoxon rank sum test with two-sided p-values. Nominal p-values with Benjamini-Hochberg (BH) corrections for $p \leq 0.05$ (CD4 + and CD8 + cells separately). Shown here graphically are box plots (generated in GraphPad Prism) defining the 25th and 75th percentile and median values and whiskers for minimum and maximum values: **a**, CD4 + clusters; **b**, CD8 + clusters; and **c**, CD3 + CD4-CD8- subsets.

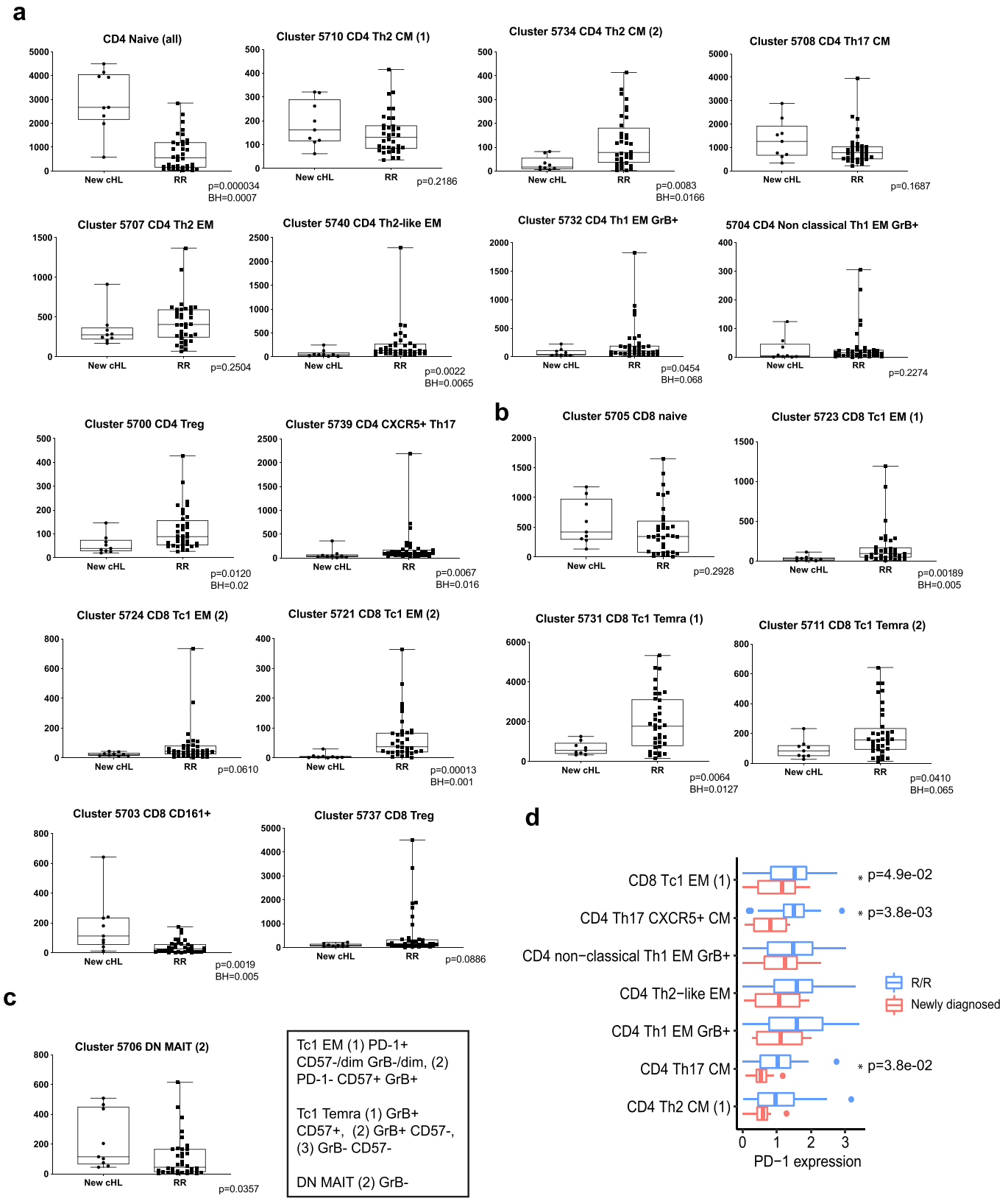

Extended Data Fig. 4 | See next page for caption.

Extended Data Fig. 4 | Comparison of CD3+ populations in patients with newly diagnosed cHL versus relapsed/refractory cHL (all) at baseline. To quantify differences between these 2 groups, newly diagnosed cHL (n = 9) and relapsed/refractory cHL (n = 36), we determined the number of cells that each sample contributed to a given cluster and applied a Wilcoxon rank sum test with two-sided p-values. Nominal p-values with Benjamini-Hochberg corrections for $p \leq 0.05$ (CD4 + and CD8 + cells separately). Shown here graphically are box plots (generated in GraphPad Prism) defining the 25th and 75th percentile and median values and whiskers for minimum and maximum values: **a**, CD4 + clusters; **b**, CD8 + clusters; and **c**, CD3 + CD4-CD8- subsets. **d**, PD-1 expression on CD3 + T cell clusters identified by Vortex in patients with newly diagnosed cHL vs. relapsed/refractory disease. Only clusters with z-score normalized PD-1 expression greater than 0 (ie. greater than the mean) in the PD-1 columns in the Fig. 3h heat-maps are shown. The differences in PD-1 expression in T-cell subsets from patients with newly diagnosed and relapsed/refractory cHL were measured by the Wilcoxon rank sum test with two-sided p-values, significance denoted by asterisks.

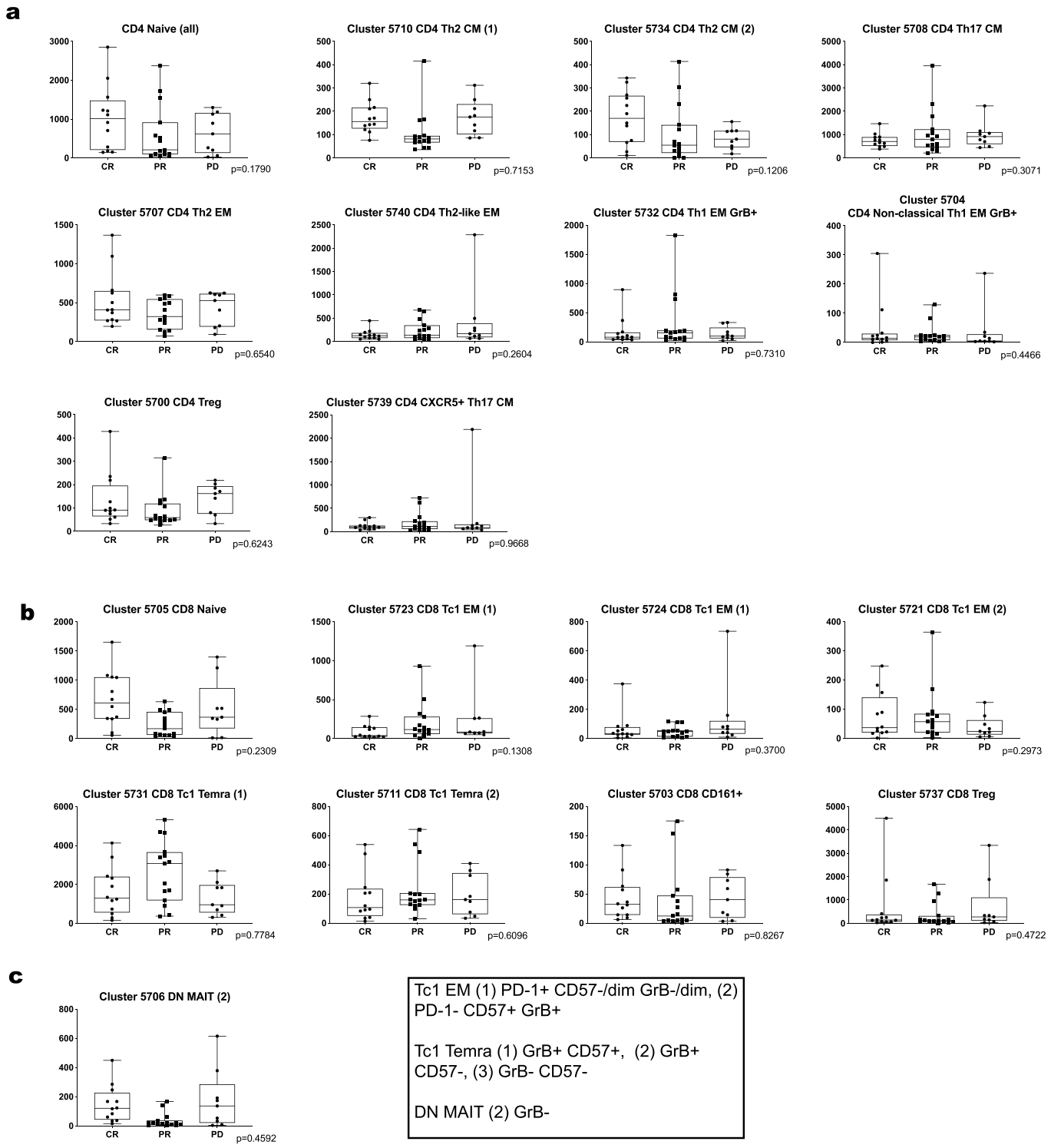

Extended Data Fig. 5 | Comparison of CD3+ populations in patients with relapsed/refractory cHL at baseline split by best overall response to subsequent PD-1 blockade (CR, PR, PD). To quantify differences between these groups, (CR n = 12, PR n = 15, PD n = 9) we determined the number of cells that each sample contributed to a given cluster and applied a Cuzick trend test (two-sided nominal p-values). Shown here graphically are box plots (generated in GraphPad Prism) defining the 25th and 75th percentile and median values and whiskers for minimum and maximum values: **a**) CD4 + clusters; **b**) CD8 + clusters; and **c**) CD3 + CD4-CD8- subsets.

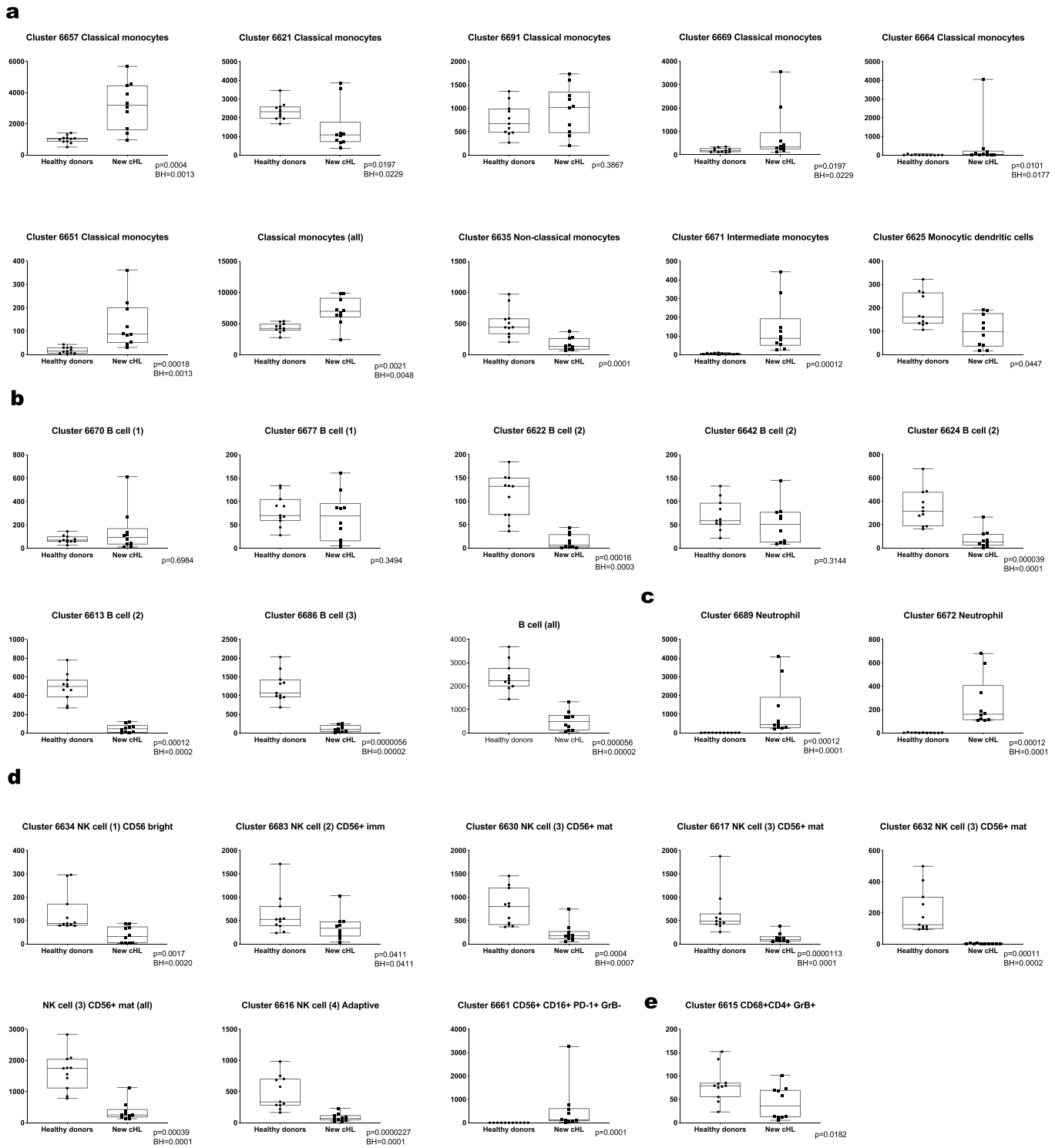

Extended Data Fig. 6 | Comparison of CD3- populations in healthy donors versus patients with newly diagnosed cHL. To quantify differences between these 2 groups, patients with newly diagnosed cHL (n = 10) and relapsed/refractory cHL (n = 35), we determined the number of cells that each sample contributed to a given cluster and applied a Wilcoxon rank sum test (two-sided nominal p-values) with Benjamini-Hochberg (BH) corrections for $p \leq 0.05$ (Classical Monocytes, Neutrophils, B cells and NK cells separately). One patient with newly diagnosed cHL who had sufficient numbers of CD3- sampled events in Extended Data Fig. 6–8 had insufficient numbers of CD3 + sampled events and was excluded from the CD3 + analysis in Extended Data Figs. 3–5). One patient with relapsed/refractory cHL had sufficient numbers of CD3 + sampled events for inclusion in Extended Data Figs. 4, 5 but had insufficient numbers of CD3- sampled events and was excluded from the CD3- analyses in Extended Data Fig. 6–8. Shown here graphically are box plots (generated in GraphPad Prism) defining the 25th and 75th percentile and median values and whiskers for minimum and maximum values: **a**) Monocyte clusters; **b**) B cell clusters [(1) CXCR5- CD73- IRF4-, (2) CXCR5 + CD73-IRF4-, (3)CXCR5 + CD73 + IRF4 +]; **c**) Neutrophils; **d**) NK cell clusters and **e**) CD68 + CD4 + GrB+ cells.

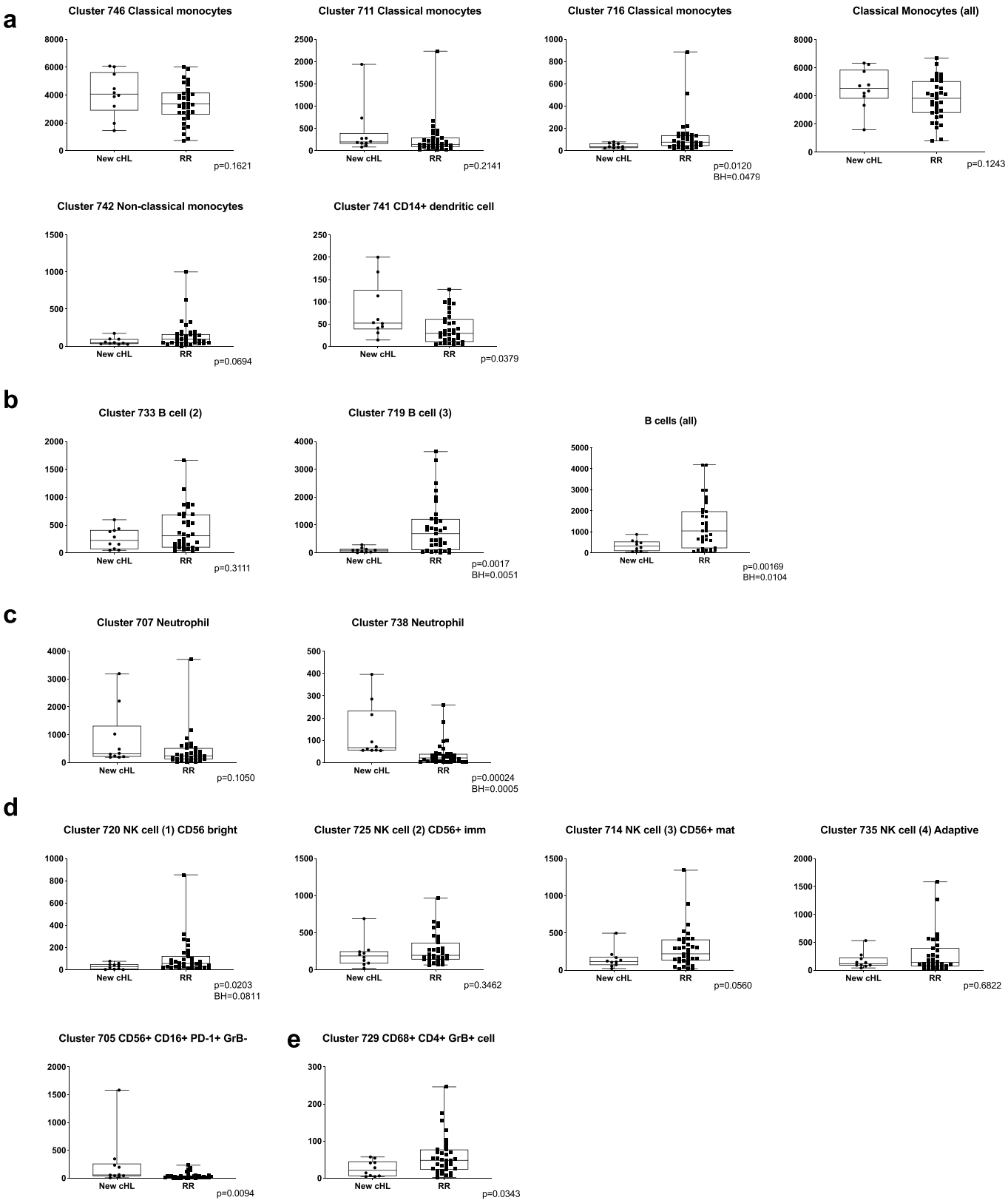

Extended Data Fig. 7 | Comparison of CD3- populations in patients with newly diagnosed cHL versus relapsed/refractory cHL (all) at baseline. To quantify differences between these 2 groups, patients with newly diagnosed cHL (n = 10) and relapsed/refractory cHL (n = 35), we determined the number of cells that each sample contributed to a given cluster and applied a Wilcoxon rank sum test (two-sided nominal p-values) with Benjamini-Hochberg (BH) corrections for $p \leq 0.05$ (Classical Monocytes, Neutrophils, B cells and NK cells separately). Shown here graphically are box plots (generated in GraphPad Prism) defining the 25th and 75th percentile and median values and whiskers for minimum and maximum values: **a**) Monocyte clusters; **b**) B cell clusters [(2) CXCR5 + CD73-IRF4-, (3) CXCR5 + CD73 + IRF4 +]; **c**) Neutrophils; **d**) NK cell clusters and **e**) CD68 + CD4 + GrB+ cells.

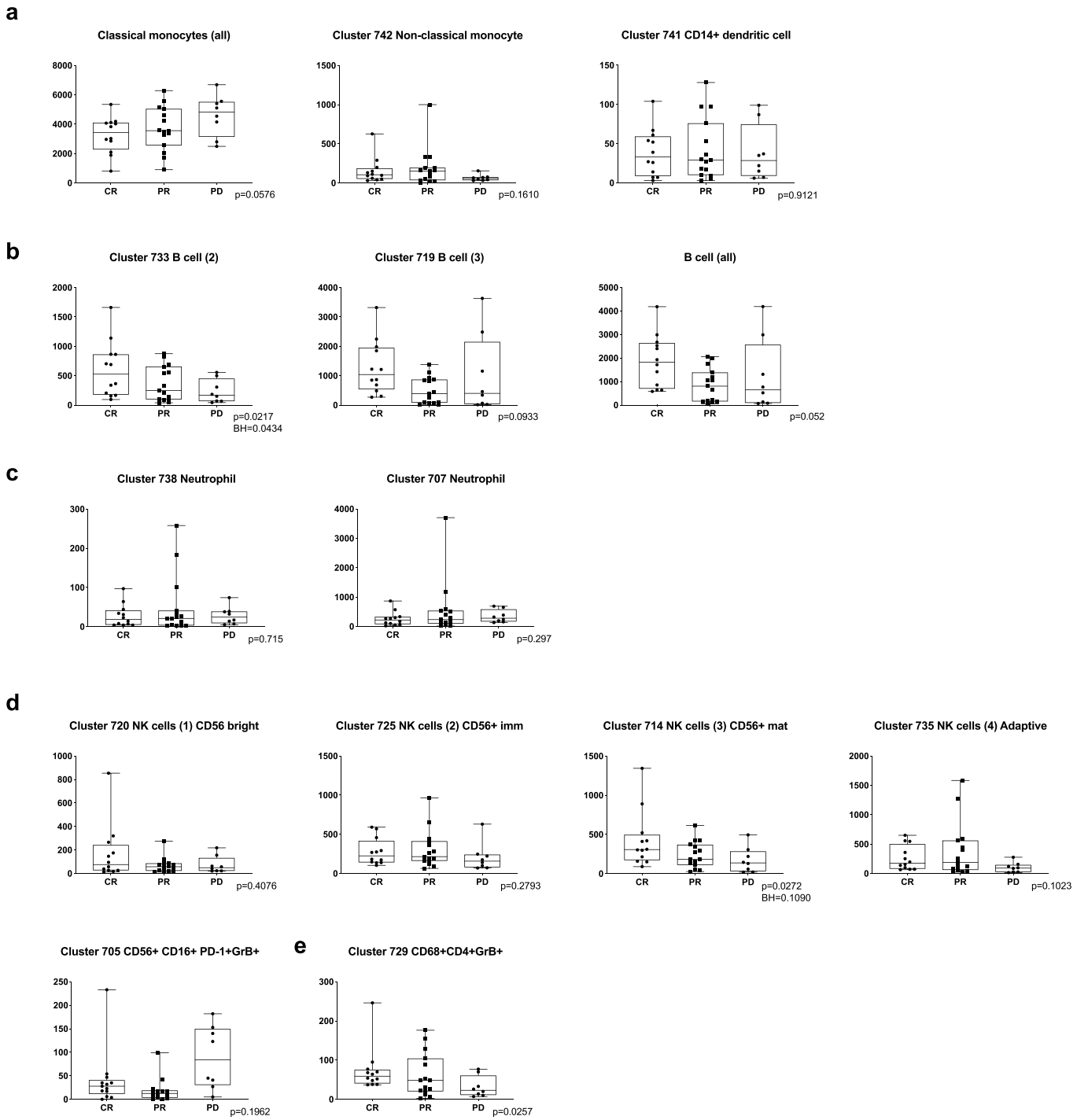

Extended Data Fig. 8 | Comparison of CD3- populations in patients with relapsed/refractory cHL split by best overall response at baseline (CR, PR, PD). To quantify differences between these groups (CR n = 12, PR n = 15, PD n = 8), we determined the number of cells that each sample contributed to a given cluster and applied Cuzick trend test (two-sided nominal p-values) with Benjamini-Hochberg (BH) corrections for $p \leq 0.05$ (B cells and NK cells separately). Shown here graphically are box plots (generated in GraphPad Prism) defining the 25th and 75th percentile and median values and whiskers for minimum and maximum values: **a**) Monocyte clusters; **b**) B-cell clusters [(2) CXCR5 + CD73-IRF4-, (3) CXCR5 + CD73 + IRF4 +]; **c**) Neutrophils; **d**) NK-cell clusters and **e**) CD68 + CD4 + GrB+ cells.

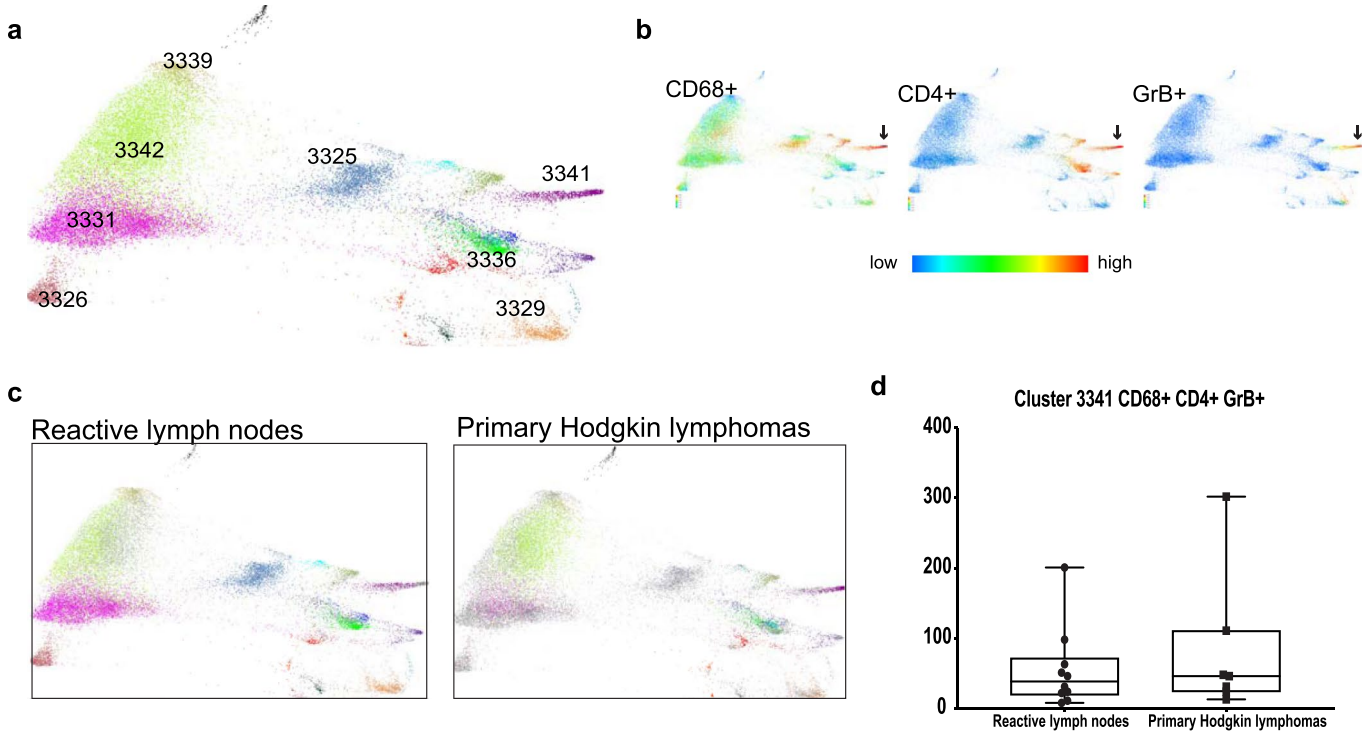

Extended data Fig. 9 | CyTOF analyses of CD3- cell populations from viable singlet cells from 7 primary cHLs and 10 reactive lymph nodes/tonsils from[31]**. a**, Force-directed layouts generated from X-shift analysis within VorteX visualization environment by sampling 4500 events from each sample and pooling resulting events together prior to clustering. The X-shift algorithm clusters events according to similarities in expression of CyTOF panel proteins, grouping events with shared lineage, differentiation and polarization within the pool. Every identified unique population is labeled with a specific color based on the Hex color code. **b**, Expression of CD68, CD4 and Granzyme B across all samples. **c**, Separate force-directed layouts (FDLs) of reactive lymph node and primary cHL cell suspensions. In each FDL, the events pertaining to the group of interest retain their Hex color code. Events belonging to the other group are represented in grey. **d**, Comparison of CD3-CD68 + CD4 + GrB+ Cluster 3341 between reactive lymph nodes and primary cHLs. Shown here graphically are box plots (generated in GraphPad Prism) defining the 25th and 75th percentile and median values and whiskers for minimum and maximum values. To quantify differences between these 2 groups, we determined the number of cells that each sample contributed to a given cluster and applied a Wilcoxon rank sum test with two-sided p-values.

nature research

Corresponding author(s): Margaret Shipp

Last updated by author(s): 29 June 2020

Reporting Summary

Nature Research wishes to improve the reproducibility of the work that we publish. This form provides structure for consistency and transparency in reporting. For further information on Nature Research policies, see our Editorial Policies and the Editorial Policy Checklist.

Statistics

For all statistical analyses, confirm that the following items are present in the figure legend, table legend, main text, or Methods section.

n/a	Confirmed	
☐	☒	The exact sample size (*n*) for each experimental group/condition, given as a discrete number and unit of measurement
☐	☒	A statement on whether measurements were taken from distinct samples or whether the same sample was measured repeatedly
☐	☒	The statistical test(s) used AND whether they are one- or two-sided *Only common tests should be described solely by name; describe more complex techniques in the Methods section.*
☐	☒	A description of all covariates tested
☐	☒	A description of any assumptions or corrections, such as tests of normality and adjustment for multiple comparisons
☐	☒	A full description of the statistical parameters including central tendency (e.g. means) or other basic estimates (e.g. regression coefficient) AND variation (e.g. standard deviation) or associated estimates of uncertainty (e.g. confidence intervals)
☐	☒	For null hypothesis testing, the test statistic (e.g. *F*, *t*, *r*) with confidence intervals, effect sizes, degrees of freedom and *P* value noted *Give P values as exact values whenever suitable.*
☒	☐	For Bayesian analysis, information on the choice of priors and Markov chain Monte Carlo settings
☒	☐	For hierarchical and complex designs, identification of the appropriate level for tests and full reporting of outcomes
☐	☒	Estimates of effect sizes (e.g. Cohen's *d*, Pearson's *r*), indicating how they were calculated

Our web collection on statistics for biologists contains articles on many of the points above.

Software and code

Policy information about availability of computer code

Data collection	1. X-shift Algorithm (version VorteX 26-Apr-2018) 2. Comparison analyses for CyTOF based experiments were performed using R (version 3.3.2) and TCR sequencing analysis (R 3.5.1 and Python 2.7.15) 3. Multispectal image analysis on Inform 2.4 (PerkinElmer) 4. Cytobank -version 6. For the CyTOF data samples, Cytobank platform was used to first manually gate and identify the relevant populations to export for analysis. The TCR sequences from peripheral bulk peripheral blood mononuclear cells and highly purified CD4+ and CD8+ T cells were processed through the immunoSEQ platform of Adaptive Biotechnologies. Image acquisition was performed using the Mantra multispectral imaging platform (PerkinElmer, Hopkinton, MA). Areas with non-tumor or residual normal tissue were excluded from the analysis. Representative regions of interest were chosen by the pathologist (S.J.R.), and 3-5 fields of view (FOVs) were acquired at 20x resolution as multispectral images. After image capture, the FOVs were spectrally unmixed and then analyzed using supervised machine learning algorithms within Inform 2.4 (PerkinElmer). Thresholds for positive staining and the accuracy of phenotypic algorithms were optimized and confirmed for each case.
Data analysis	CyTOF data was processed by VorteX (26-Apr-2018) and the output was processed by a custom R script. The TCRseq data was processed and analyzed by custom Python and R scripts. The codes are available at https://github.com/huxihao/cHL-PBMC. Cytobank provides a cloud-based software analysis and the version is continuously updated by Cytobank. The data included in this manuscript was analyzed on version 6.

For manuscripts utilizing custom algorithms or software that are central to the research but not yet described in published literature, software must be made available to editors and reviewers. We strongly encourage code deposition in a community repository (e.g. GitHub). See the Nature Research guidelines for submitting code & software for further information.

Data

Policy information about availability of data

All manuscripts must include a data availability statement. This statement should provide the following information, where applicable:

- Accession codes, unique identifiers, or web links for publicly available datasets
- A list of figures that have associated raw data
- A description of any restrictions on data availability

The TCR sequences for this study were processed through the immunoSEQ platform of Adaptive Biotechnologies and will be made publicly available after publication. The DOI for our data will be 10.21417/FZC2020NM and the URL will be https://adaptivebiotech.com/pub/cader-2020-nm.
Source FCS files used in the CyTOF analyses will be made publicly available through login at Cytobank. This can be accessed at https://premium.cytobank.org/cytobank/experiments#project-id=2539 and https://premium.cytobank.org/cytobank/experiments/310927.

Field-specific reporting

Please select the one below that is the best fit for your research. If you are not sure, read the appropriate sections before making your selection.

☒ Life sciences ☐ Behavioural & social sciences ☐ Ecological, evolutionary & environmental sciences

For a reference copy of the document with all sections, see nature.com/documents/nr-reporting-summary-flat.pdf

Life sciences study design

All studies must disclose on these points even when the disclosure is negative.

Sample size	We obtained baseline and on-treatment cryopreserved peripheral blood mononuclear cells (PBMCs) from 56 patients who received anti-PD-1 therapy (nivolumab) on the Checkmate 205 clinical trial. This multi-center, multi-cohort phase II study included patients with relapsed/refractory cHL following autologous stem cell transplantation (ASCT) alone (Cohort A) or ASCT and brentuximab vedotin (BV) (Cohorts B and C). PBMCs were collected immediately before the initiation of therapy (cycle 1 day 1 [C1D1]) and at two timepoints during PD-1 blockade, cycle 2 day 1 (C2D1) and cycle 4 day 1 (C4D1). In addition, cryopreserved PBMCs were obtained from 11 patients with newly diagnosed, previously untreated cHL and 17 healthy donors for comparison (Online Methods and Supplemental data Table 1). The sample sizes were sufficient to analyze meaningful differences in the available cohorts.
Data exclusions	To avoid the confounding variable of ongoing immune reconstitution, we restricted our subsequent analyses to patients who were treated with nivolumab ≥ 1 year following myeloablative ASCT. Seven separate X-shift analyses were performed: (1) CD3+ cells and (2) CD3- cells from healthy donors and patients with newly diagnosed cHL, sampling 12000 events; (3) CD3+ cells and (4) CD3- cells from patients with newly diagnosed and relapsed/refractory cHL, sampling 7500 events, and (5) CD3+ cells and (6) CD3- cells from all cases, sampling 7500 events. Lastly, (7) CD3- cells from a previous CyTOF analysis of normal reactive lymph nodes and primary cHL suspensions were analyzed, sampling 4500 events based on available cell counts from the smallest specimen. For analyses (3) and (4), only patients with relapsed/refractory cHL who initiated PD-1 blockade > 12 months from completion of ASCT were included. Data interpretation for analyses (5) and (6) was restricted to patients with a greater than 12 month interval between their prior myeloablative ASCT and study therapy (nivolumab) who had paired Cycle 1 Day 1 (C1D1) and Cycle 4 Day 1 (C4D1) samples.
Replication	No replication possible as study used clinical trial samples.
Randomization	Patients were recruited to the associated clinical trial of PD-1 blockade, Checkmate 205 and analysis was done based on best overall response. Armand, P., et al. Nivolumab for Relapsed/Refractory Classic Hodgkin Lymphoma After Failure of Autologous Hematopoietic Cell Transplantation: Extended Follow-Up of the Multicohort Single-Arm Phase II CheckMate 205 Trial. J Clin Oncol 36, 1428-1439 (2018).
Blinding	Both TCRseq and CyTOF data acquisition were performed blinded to clinical parameters.

Reporting for specific materials, systems and methods

We require information from authors about some types of materials, experimental systems and methods used in many studies. Here, indicate whether each material, system or method listed is relevant to your study. If you are not sure if a list item applies to your research, read the appropriate section before selecting a response.

Materials & experimental systems

n/a	Involved in the study
☐	☒ Antibodies
☒	☐ Eukaryotic cell lines
☒	☐ Palaeontology and archaeology
☒	☐ Animals and other organisms
☐	☒ Human research participants
☐	☒ Clinical data
☒	☐ Dual use research of concern

Methods

n/a	Involved in the study
☒	☐ ChIP-seq
☒	☐ Flow cytometry
☒	☐ MRI-based neuroimaging

Antibodies

Antibodies used

CyTOF antibody table removed from methods section and made into Supplemental Table 2 with an update to include catalogue number and dilution.

CyTOF antibodies
CD45 Fluidigm/ DVS sciences HI30 89Y
PAX5 Biolegend IH9 113Ind
CD14 Biolegend M5E2 115Ind
Eomes eBioscience WD1928 141Pr
Ki-67 BD Biosciences B56 142Nd
CD30 BD biosciences BerH8 143Nd
CCR5 Fluidigm/ DVS sciences NP-6G4 144Nd
CD4 Fluidigm/ DVS sciences RPA-T4 145Nd
CD8a Fluidigm/ DVS sciences RPA-T8 146Nd
cParp BD Biosciences F21-852 147Sm
HLA-A/B/C (MHC class I) Biolegend W6/32 148Nd
CD25 Fluidigm/ DVS sciences 2A3 149Sm
CD57 Biolegend HCD57 150Nd
Tim3 BD biosciences 7D3 151Eu
PD-L2 Courtesy of G.Freeman, DFCI 24F.10C12 152Sm
pSTAT1 Fluidigm/ DVS sciences 4a 153Eu
CD163 Fluidigm/ DVS sciences GHI/61 154Sm
PD-1 Courtesy of G.Freeman, DFCI EH12.2H7 155Gd
B2M Biolegend 2M2 156Gd
CCR4 Fluidigm/ DVS sciences 205410 158Gd
CCR7 Fluidigm/ DVS sciences G043H7 159Tb
T-bet Fluidigm/ DVS sciences 4B10 160Gd
PD-L1 Courtesy of G.Freeman, DFCI 29E.2A3 161Dy
FoxP3 Fluidigm/ DVS sciences PCH101 162Dy
CXCR5 BD biosciences 51505 163Dy
CD161 Fluidigm/ DVS sciences HP-3G10 164Dy
CD45RO Fluidigm/ DVS sciences UCHL1 165Ho
Lag3 R&D 874501 166Er
Granzyme B Harvard Medical School GB11 167Er
CD73 Fluidigm/ DVS sciences AD2 168Er
CD33 Fluidigm/ DVS sciences WM53 169Tm
CD3 Fluidigm/ DVS sciences UCH T 1 170Er
CD68 Fluidigm/ DVS sciences Y1/82a 171Yb
phosphoS6 Cell Signaling Technologies D57.2.2E 172Yb
IRF4 Biolegend IRF4.3E4 173Yb
HLA-DR/DP/DQ (MHC class II) Biolegend Tu39 174Yb
CD15 Biolegend HI98 175Lu
CD56 BD Biosciences B159 176Yb
CD16 Fluidigm/ DVS sciences 3G8 209Bi
CD3 1:750 Poly ref# A0452 lot# 20068607 Dako 650
CD4 1:250 4B12 ref# M7310 lot#20061090 Dako 520
CD68 1:2000 PGM1 ref#M0876 lot#20024189 Dako 620
PAX5 1:100 24/Pax-5 ref#610863 lot#9017823 BD Biosciences 570
GZMB 1:100 Grb-7 ref#M7235 lot#20036875 Dako 540

Validation

CyTOF antibody validation described in Cader, F.Z., et al. Mass cytometry of Hodgkin lymphoma reveals a CD4(+) regulatory Tcell-rich and exhausted T-effector microenvironment. Blood 132, 825-836 (2018).
IF antibody validation described in Carey, C.D., et al. Topological analysis reveals a PD-L1-associated microenvironmental niche for Reed-Sternberg cells in Hodgkin lymphoma. Blood 130, 2420-2430 (2017).

Human research participants

Policy information about studies involving human research participants

Population characteristics	For the number of past treatments for clinical trial patients, information is provided in Supplemental Table 1. No additional covariate population characteristics were utilized.
Recruitment	Patients were recruited to the associated clinical trial of PD-1 blockade, Checkmate 205. Armand, P., et al. Nivolumab for Relapsed/Refractory Classic Hodgkin Lymphoma After Failure of Autologous Hematopoietic Cell Transplantation: Extended Follow-Up of the Multicohort Single-Arm Phase II CheckMate 205 Trial. J Clin Oncol 36, 1428-1439 (2018).
Ethics oversight	The IRB at each institution participating in the CheckMate 205 clinical trials (Armand, P., et al. Nivolumab for Relapsed/ Refractory Classic Hodgkin Lymphoma After Failure of Autologous Hematopoietic Cell Transplantation: Extended Follow-Up of the Multicohort Single-Arm Phase II CheckMate 205 Trial. J Clin Oncol 36, 1428-1439 (2018)) approved the banking of PBMC samples for associated research studies. The Dana-Farber Cancer Institute IRB also approved the laboratory research studies. Samples from normal healthy donors were obtained under an umbrella protocol for otherwise discarded anonymized tissues.

Note that full information on the approval of the study protocol must also be provided in the manuscript.

Clinical data

Policy information about clinical studies

All manuscripts should comply with the ICMJE guidelines for publication of clinical research and a completed CONSORT checklist must be included with all submissions.

Clinical trial registration	ClinicalTrials.gov identifier: NCT02181738
Study protocol	The clinical trial has been completed and is described in Armand, P., et al. Nivolumab for Relapsed/Refractory Classic Hodgkin Lymphoma After Failure of Autologous Hematopoietic Cell Transplantation: Extended Follow-Up of the Multicohort Single-Arm Phase II CheckMate 205 Trial. J Clin Oncol 36, 1428-1439 (2018).
Data collection	Peripheral blood mononuclear samples were collected at Cycle 1 day1, Cycle 2 day 1 and Cycle 4 day1 from patients at each of the participating institutions subsequently sent to the sponsor of the clinical trial (Bristol Myers Squibb).
Outcomes	The primary and secondary outcomes of the Checkmate 205 clinical trial are reported in Armand et al (above). Best overall response data are from the May 2018 data lock.